Chem Soc Rev

Confinement-Guided Photophysics in MOFs, COFs, and Cages

Journal:	*Chemical Society Reviews*
Manuscript ID	CS-REV-12-2020-001519.R1
Article Type:	Review Article
Date Submitted by the Author:	12-Jan-2021
Complete List of Authors:	Leith, Gabrielle; University of South Carolina, Department of Chemistry and Biochemistry Martin, Corey; University of South Carolina, Department of Chemistry and Biochemistry Mayers, Jacob; University of South Florida, Kittikhunnatham, Preecha; University of South Carolina, Chemistry and Biochemistry Larsen, Randy; University of South Florida, Chemistry Shustova, Natalia; University of South Carolina, Chemistry and Biochemistry

ARTICLE

Confinement-Guided Photophysics in MOFs, COFs, and Cages

Gabrielle A. Leith,[‡a] Corey R. Martin,[‡a] Jacob M. Mayers,[‡b] Preecha Kittikhunnatham,[a] Randy W. Larsen,[*b] and Natalia B. Shustova[*a]

Received 00th January 20xx,
Accepted 00th January 20xx

DOI: 10.1039/x0xx00000x/

In this review, the dependence of the photophysical response of chromophores in the confined environments associated with crystalline scaffolds, such as metal-organic frameworks (MOFs), covalent-organic frameworks (COFs), and molecular cages, has been carefully evaluated. Tunability of the framework aperture, cavity microenvironment, and scaffold topology significantly affects emission profiles, quantum yields, or fluorescence lifetimes of confined chromophores. In addition to the role of the host and its effect on the guest, the methods for integration of a chromophore (e.g., as a framework backbone, capping linker, ligand side group, or guest) are discussed. The overall potential of chromophore-integrated frameworks for a wide-range of applications including artificial biomimetic systems, white-light emitting diodes, photoresponsive devices, and fluorescent sensors with unparalleled spatial resolution are highlighted throughout the review.

1. Introduction

Photophysical properties can substantially affected by a confined space, resulting in drastic changes in physicochemical properties of molecules including excited-state molecular dynamics, electronic structure, and reaction kinetics.[1–6] Over the years, the broader scientific community has shown a growing interest in chromophore dynamics in areas such as materials science and supramolecular chemistry.[7–12] For instance, chromophore integration inside a rigid scaffold can lead to remarkable changes in the emission/absorption maxima, quantum yields (QYs) and/or fluorescence lifetimes (i.e., chromophore@host versus unrestricted chromophore).[13–19] In this review, we focus on the role of a confined space of metal-organic frameworks (MOFs), covalent-organic frameworks (COFs), and molecular cages (metal-organic polyhedra (MOPs)) on chromophore molecular conformations and the photophysical properties that can arise (Scheme 1). For instance, there have already been numerous experimental studies highlighting the advantages of a controlled environment on energy transfer (ET), photoluminescence, and conformational dynamics.[20–27]

Crystalline porous structures, e.g., MOFs and COFs, have wide-spread applications spanning from the "classical" realm such as gas storage and separation to avant-garde such as protein encapsulation for catalysis.[28–47] The judicious choice of metals and organic linkers in MOFs or just linkers in COFs, allows for enabling strategic control over structural design.[48–51] For instance, the nearly limitless choice of building blocks enable design of MOFs and COFs with various pore sizes, surface areas, and functionalities, thus allowing for systematic investigations of the effect a confined space imposes on a chromophore. Similarly, coordination cages have a variety of organic linkers and metals to choose from, but they form discrete structures rather than extended motifs.[51] The difference in structural features results in the possibility to study cages (and therefore, integrated chromophores) through conventional techniques such as solution-based nuclear magnetic resonance (NMR) spectroscopy. Moreover, they can be used to mimic the environment of MOF pores, allowing for analysis of a chromophores conformation by single crystal X-ray diffraction (SC-XRD).[52,53] Similar studies in MOFs can be challenging due

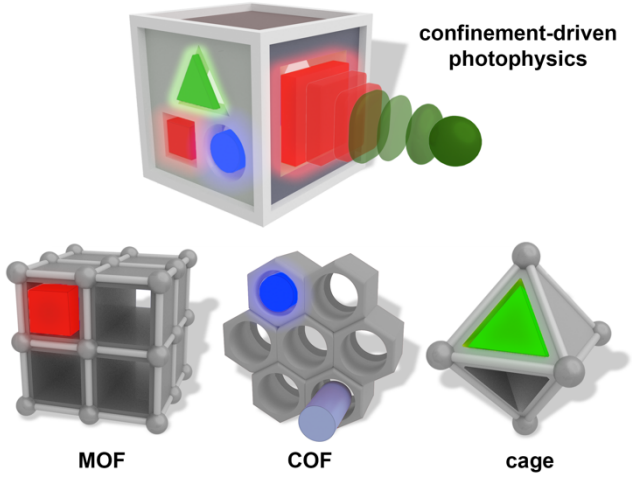

Scheme. 1 Schematic representation of the effect of a confined space on the example of MOFs, COFs, and cages. Reproduced from ref. 53 with permission from American Chemical Society, copyright 2020.

[a] *Department of Chemistry and Biochemistry, University of South Carolina, Columbia, South Carolina 29210, United States*
[b] *Department of Chemistry, University of South Florida, Tampa, Florida 33620, United States*
‡ These authors contributed equally.
*Corresponding authors
Emails: rwlarsen@usf.edu; shustova@sc.edu

to severe crystallographic disorder of integrated guest molecules.

This review will exclusively focus on the effect that the confined space of MOFs, COFs, and cages has on the photophysics of chromophores embedded as guests and as linkers. In particular, studies appraising the incorporation of benzylidene imidazolone (BI)-based chromophores, photochromic molecules, and transition metal polyimines, as well as chromophore incorporation in crystalline scaffolds that would otherwise exhibit aggregation-caused quenching (ACQ) in the solid state or aggregation-induced emission (AIE) when low-energy vibrational modes are restricted, will be presented.

2. Confinement-Driven Guest Photophysics

The host-guest platform, such as guest-loaded MOFs and COFs, provides an opportunity to study the effect that confinement (e.g., host-guest interactions and solvent effects) has on chromophore photophysics. For example, there are distinct differences in emission profiles, fluorescence lifetimes, and QYs of chromophores aggregated in the solid state versus ones spatially separated within a rigid matrix.[13,14,54] Porous frameworks and cages are also versatile platforms for probing the confinement effect by tuning a diverse array of parameters. For example, modulating topology can lead to an increase in pore size and can result in changes in guest molecular conformation as well as host-guest interactions.[53] Similarly, chromophores located inside a porous host and surrounded by polar solvent molecules can display bathochromic shifts in emission profiles.[55]

Overall, integration of a chromophore as a guest inside a rigid scaffold is a convenient way to achieve and study photophysics modulation. In other words, this method is advantageous since encapsulation of guests in porous frameworks does not typically rely on labor-intensive chromophore derivatization. In fact, there are a myriad of chromophores commercially available that can be incorporated as guests without any modification, in comparison with a multi-step synthesis required for scaffold linker design. This section will be devoted to a discussion based on tailoring the photophysics of a chromophore as a guest within a confined porous scaffold (Fig. 1).

2.1 Guests Chromophores with Benzylidene Imidazolone Cores

Fluorescent proteins are employed for applications including biomarkers and biosensors to monitor reaction progress *in vivo* as well as to detect specific ions or reactive oxygen species.[56,57] One renowned example of fluorescent proteins is the green fluorescent protein (GFP) that has attracted considerable attention since its discovery.[58] The photoluminescence properties of GFP rely on the HBI (HBI = 5-

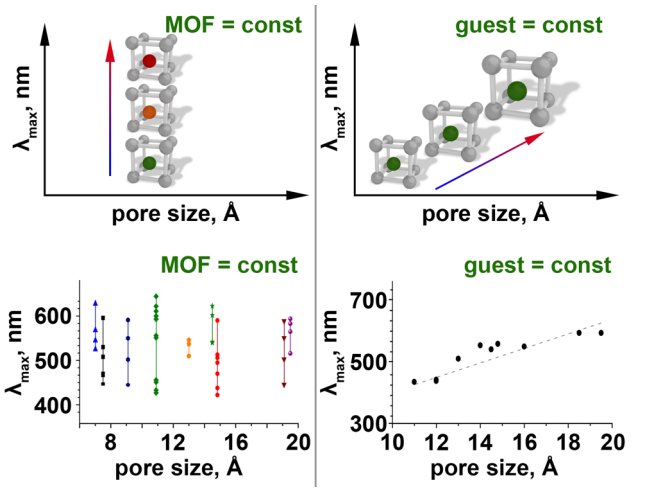

Fig. 1 Schematic representation of emission maxima for encapsulated chromophores as a function of (*top left*) a guest chromophore (MOF = constant, guest = variable) and (*top right*) a framework pore size (guest = constant, MOF = variable). Literature analysis of dependence of the guest@MOF emission maximum as a function of the framework pore size: (*bottom left*) MOF = constant, guest = variable and (*bottom right*) MOF = variable, guest = constant. Reproduced from ref. 53 with permission from American Chemical Society, copyright 2020.

(4-hydroxybenzylidene)-3,5-dihydro-4*H*-imidazol-4-one; Fig. 2) chromophore being tightly surrounded by a protein *β*-barrel, thus, reducing excited state relaxation pathways (i.e., nonradiative decay) such as twisting, rotating, or tilting (e.g., "hula-twist").[59–61] The confined environment of the *β*-barrel is crucial for fluorescence to occur and the release of the HBI chromophore from GFP results in a four-orders-of-magnitude decrease in fluorescence QY.[60,61] One method to address the challenge of low QYs of BI-based chromophores outside of the protein *β*-barrel is to synthetically mimic the confined space of the protein using, for instance, another rigid scaffold (e.g., MOFs, COFs, or cages) to suppress non-radiative decay pathways.

There are primarily two conceptually different approaches for tuning photoluminescence of MOFs using guest molecules as shown in Fig. 1.[53] In the first approach, the emission maxima of guest@MOF spectra can be varied in a wide range due to integration of different chromophores inside the same MOF, i.e., MOF is a constant while the encapsulated chromophore varies. The second approach is based on the opposite concept in which the embedded guest is constant while the MOF is varied, i.e., the same chromophore is incorporated into different scaffolds that allows for tailoring the photoluminescent response. Shustova and coworkers applied both approaches for tuning fluorescence over a wide emission range by derivatizing the BI-chromophore core with electron-donating and electron-withdrawing groups (EDG and EWG,

respectively) or halogens (Fig. 1, approach 1 and Fig. 2).[62] The prepared chromophores were integrated as guests inside a framework, i.e., the first approach mentioned above (Fig. 1). For instance, the authors incorporated seven chromophores BI, (BI = 5-benzylidene-2,3-dimethyl-3,5-imidazol-4-one; Fig. 2), *p*MBI (*p*MBI = 4-methylbenzylidene-2,3-dimethylimidazol-4-one; Fig. 2), EC-*o*HBI (EC-*o*HBI = ethyl-3-((1,2-dimethyl-5-oxo-imidazol-4-ylidene)methyl)-4-hydroxybenzoate; Fig. 2), NO_2-*o*HBI (NO_2-*o*HBI = 5-(2-hydroxy-5-nitrobenzylidene)-2,3-dimethyl-imidazol-4-one; Fig. 2), Br-*o*HBI (Br-*o*HBI = 5-(5-bromo-2-hydroxybenzylidene)-2,3-dimethyl-imidazol-4-one; Fig. 2), and *o*HBI (*o*HBI = 5-(2-hydroxybenzylidene)-2,3-dimethyl-imidazol-4-one); Fig. 2) into the confined environment of $Zn_3(BTC)_2$ (HKUST-1(Zn); H_3BTC = benzene-1,3,5-tricarboxylic acid) that led to emission maximum variation from 449 nm to 601 nm (Fig. 2). Interestingly, the recorded emission maxima matched ones known for the natural proteins (Fig. 2). As one of the main conclusions, the Shustova group revealed that photophysical properties could be systematically tuned through attachment of EDG, EWG, or halogens in the para position, relative to the hydroxyl group (Fig. 2, *o*-HBI compared to EC-*o*HBI, NO_2-*o*HBI, and Br-*o*HBI). For instance, photoluminescence maxima of EC-*o*HBI@ $Zn_3(BTC)_2$ and NO_2-*o*HBI@$Zn_3(BTC)_2$ are hypsochromically shifted compared to Br-*o*HBI@$Zn_3(BTC)_2$.

The same group applied the aforementioned second approach (Fig. 1) to tailor the emission profile of MOFs.[53] In this case, Cl-BI (5-(3-chlorobenzylidene)-2,3-dimethyl-3,5-dihydro-4*H*-imidazol-4-one) was chosen for systematic changes of emission profiles as a function of MOF pore aperture.[53] The established correlation between emission maximum and the pore size is show in Fig. 1 that was further corroborated with previously reported data for MeO-*o*HBI@MOF (MeO-*o*HBI = 5-(2-hydroxy-5-methoxybenzylidene)-2,3-dimethyl-3,5-dihydro-4*H*-imidazol-4-one).[22] As a result of framework variation, the emission maximum of Cl-BI@MOF can be bathochromically shifted up to 150 nm.[22,53] Building upon this work, the same group endeavored to shed light on the photophysics and dynamics of BI-based chromophores through non-coordinative inclusion in eight frameworks with a variety of topologies and pore apertures ranging from 8 Å to 25 Å (Fig. 2, approach 2).[53] In this case, MeO-*o*HBI was chosen as a chromophore due to its sensitivity to the local environment manifested through a hypsochromic shift in emission up to 141 nm in comparison to the emission in the solid state for the same chromophore (λ_{max} = 649 nm, λ_{ex} = 350 nm).

Despite precise tuning of MOF photoluminescence through guest incorporation, one potential drawback for using periodic scaffolds for systematic studies: utilization of SC-XRD is necessary to build a correlation between a chromophore molecular conformation inside a framework and changes in guest@MOF emission profile. This issue arises from significant disorganization of guest molecules inside a framework that causes severe crystallographic disorder. To overcome this

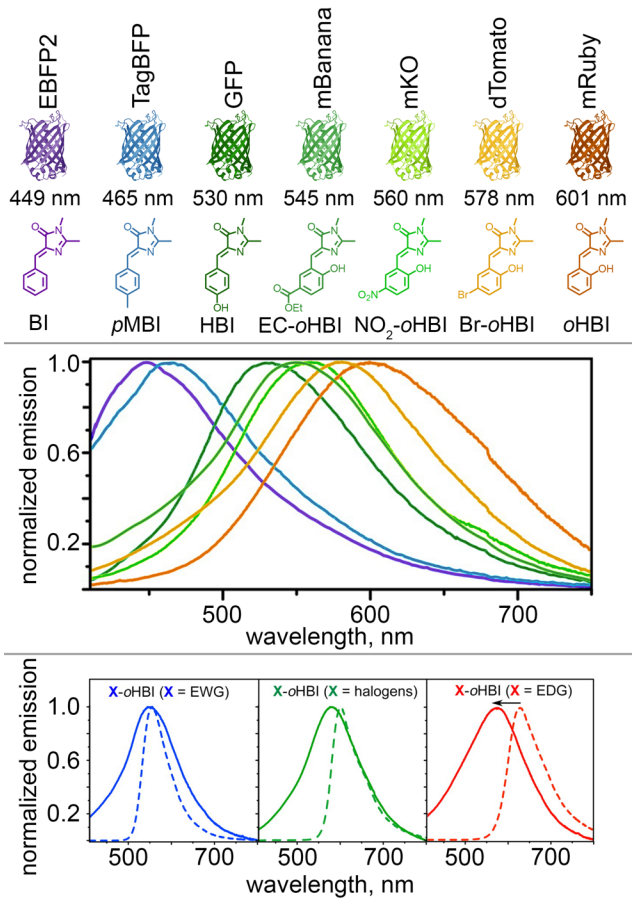

Fig. 2 (*top*) Color profile of fluorescent proteins and the BI-chromophores mimicking the photophysical profile of natural proteins. (*middle*) Normalized emission spectra of BI-based chromophores incorporated inside of $Zn_3(BTC)_2$ as a guest. (*bottom*) Normalized emission spectra of BI-derivatives with an electron-withdrawing group (EWG) (blue solid line), halogen (green solid line), and electron-donating group (EDG) (red solid line) incorporated inside of $Zn_3(BTC)_2$ and the corresponding "free" chromophores (dotted lines). Reproduced from ref. 65 with permission from American Chemical Society, copyright 2016.

challenge, a molecular cage can be utilized as a truncated model of a MOF can be utilized.[52,63,64] For instance, loading of Cl-*o*HBI (Cl-*o*HBI = 5-(5-chloro-2-hydroxybenzylidene)-2,3-dimethyl-3,5-dihydro-4*H*-imidazol-4-one) in $Pd_6(TPT)_4(NO_3)_{12}$ (TPT = 2,4,6-tri(pyridin-4-yl)-1,3,5-triazine) allowed for determination of chromophore molecular conformation (details will be described in section 4 that has a main focus on molecular cages) and therefore, building of a correlation between molecular conformation of Cl-*o*HBI and material photophysical response.[53]

Based on the acquired photophysical information of BI-related chromophores, the Shustova group has started to apply the gained knowledge to study and model Förster resonance ET processes.[66] Tunability of a scaffolds absorption and emission profiles though guest incorporation can result in the possibility for achieving spectral overlap of donor (emission) and acceptor profiles though guest incorporation can result in the possibility

for achieving spectral overlap of donor (emission) and acceptor (absorption) required for efficient ET.[67,68] Although an understanding of light-harvesting and ET processes in MOFs have progressed significantly over the years, there is still a lack of mechanistic understanding of directionality of ET in MOFs.[68–70] Shustova and coworkers used a pair of chromophores with BI and porphyrin cores as a model system to tune ET efficiency.[66] Inspired by the reported didomain bio-system,[66] they attempted to tune the structures of a BI-donor and porphyrin-acceptor to achieve the required donor-acceptor spectral overlap through utilizing the confined environment of a Pb_2(TCPP) framework (H_4TCPP = tetrakis(4-carboxyphenyl)porphyrin).[66] The relatively small one-dimensional MOF channels (11 Å) promoted incorporation of approximately one BI guest per two $TCPP^{4-}$ units, resulting in a 72% ET efficiency.[66] Discussion of coordinative immobilization of BI into the confined environment of Pb_2(TCPP) will be presented in section 3.1. Further exploration of chromophore modulation as a function of MOF geometry can potentially address the challenge of emission tunability in the near-infrared (IR) region that typically requires relatively challenging chromophore derivatization.

2.2 Photochromic Guests

Incorporation of photoresponsive chromophores as a guest into a crystalline framework provides an additional avenue for tuning framework photophysics through application of an external stimuli (e.g., light).[71–74] Moreover, the confined space of a MOF can evoke intriguing properties such as size-selective photochromic behavior,[75] X-ray induced photochromism,[76] or linear dichroism.[77] Although there are a variety of photochromic compounds incorporated in MOFs (e.g., naphthalenediimide or methyl viologen), several recent reviews highlight photochromic MOF-based photophysics[74,78] which will not be extensively discussed here. In this review, three different classes of photoswitchable molecules will be presented: azobenzene, diarylethene, and spiropyran (Fig. 3). Inclusion of photoresponsive molecules as non-coordinative guests into MOFs is advantageous since it imposes less geometrical restrictions than solid-state packing and does not require derivatization of complex photochromic cores, while still providing the advantages of a crystalline motif (e.g., spatial separation and resistance to photobleaching).[74]

Azobenzene dyes and their *E*/*Z* isomerization is often referred to as the archetype of photochromism.[79] Successful encapsulation of azobenzene into porous matrices has been demonstrated over the years.[80] However, reversible and complete azobenzene photoisomerization from the *E* to *Z* form has only recently been addressed.[81] Ruschewitz and coworkers addressed this problem by fluorinating the phenyl rings of the azobenzene followed by its incorporation inside a framework (Fig. 4).[81] In particular, integration of *tf*-AZB (*tf*-AZB = *o*-

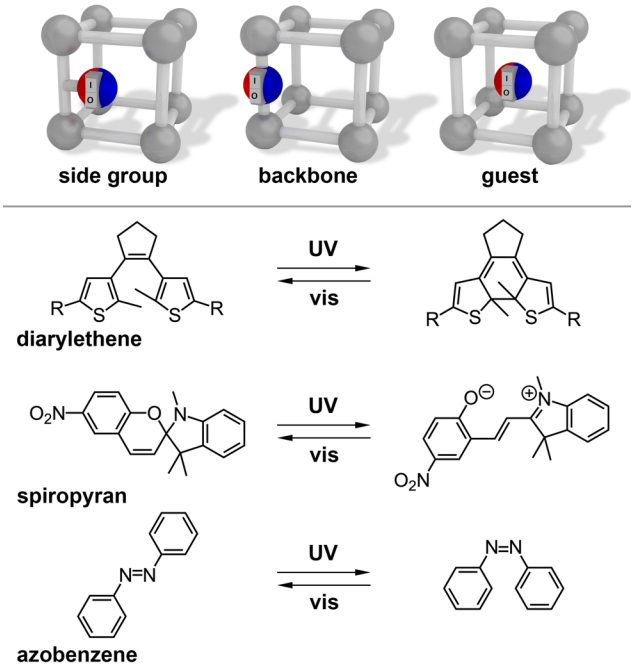

Fig. 3 Photoresponsive molecules integrated inside a framework as: (*left to right*) a side group, a backbone, and a guest. (*bottom*) Classes of photoresponsive moieties discussed in this review.[74,81–87]

tetrafluoroazobenzene; Fig. 4) as guests into MIL-68(In) (MIL = Materials Institute Lavoisier) led to an almost quantitative switching between *E* and *Z* photoisomers in the solid state and did not exhibit fatigued behavior after three switching cycles (Fig. 4). Moreover, photoisomerization could be induced with green and blue light rather than UV light that is typically used to trigger photoisomerization of azobenzene. Spectroscopic analysis of *tf*-AZB@MOF systems revealed that the IR frequencies of O–H stretching vibrations of the MOF shifted significantly upon photoisomerization, indicating a change of

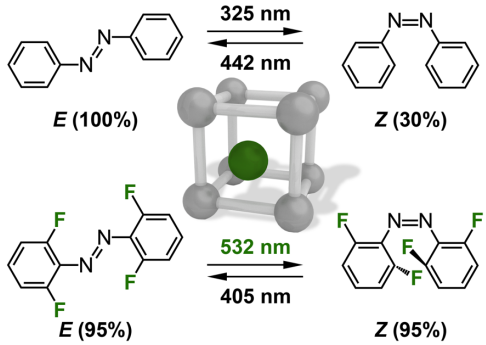

Fig. 4 (*top*) Azobenzene and (*bottom*) fluorinated azobenzene (*tf*-AZB) guests incorporated within the MIL-68(In) framework. The respective photoisomerization yields are listed under each isomer. Reproduced from ref. 81 with permission from John Wiley and Sons, copyright 2019.

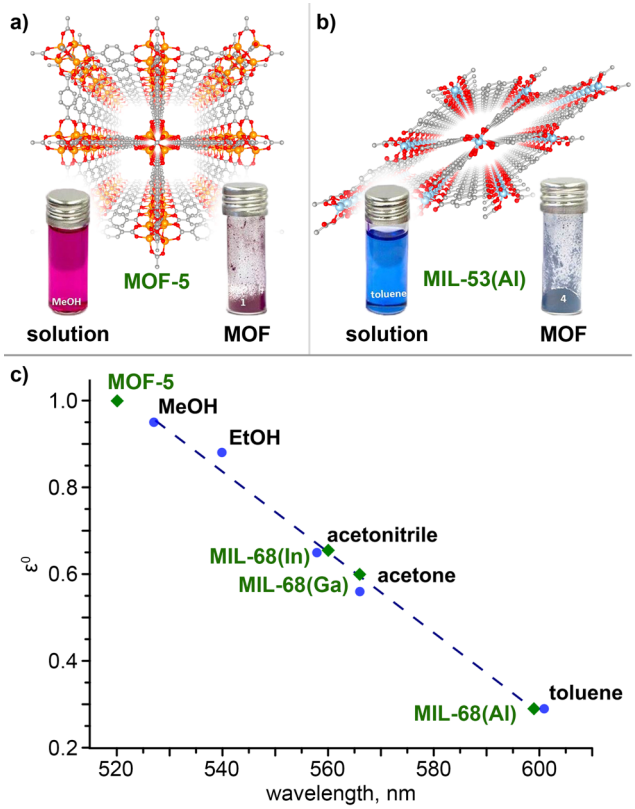

Fig. 5 (*top*) X-ray crystal structure of (a) MOF-5 and (b) MIL-53(Al) with images of the spiropyran-loaded MOF powders and respective colored solutions of chromophores. (*bottom*) Correlation of the absorption maxima of merocyanine in varying solvents (blue dots) and the reflection minima of spiropyran-loaded MOF systems (green diamonds) against the elution power (ε^0). The orange, light blue, gray, and red spheres represent Zn, Al, C, and O atoms, respectively. H atoms were omitted for clarity. Reproduced from ref. 88 with permission from American Chemical Society, copyright 2017.

intermolecular interactions of guest molecules in the confined space upon *E*/*Z* photoisomerization. Furthermore, they determined that the photochromic properties of the guest inside a framework were affected by the MOF topology, degree of guest loading, and by the chemical environment of the pore itself. The same group also ventured into encapsulation of another class of photochromic molecule, SP (SP = 1,3,3-trimethylindolino-6'-nitrobenzopyrylospiran; Fig. 3), belonging to the spiropyran family of derivatives.[88] The authors primarily monitored switching behavior spectroscopically, surveying the local reflection minimum between 500 and 600 nm of SP@MOF systems. They determined that the reflection minima could shift depending on the polarity of the host. Embedding SP in several MOFs led to the establishment of a correlation between MOF pore polarity and reflection minima of the photoresponsive MOFs (Fig. 5).

Benedict and coworkers prepared the first MOF with a diarylethene derivative as a photochromic guest (Fig. 6).[89] Upon irradiation of 1,2-bis(2,5-dimethyl-thien-3-yl)perfluorocyclopentene@$Zn_2(BDC)_2(DABCO)$ (H_2BDC = 1,4-

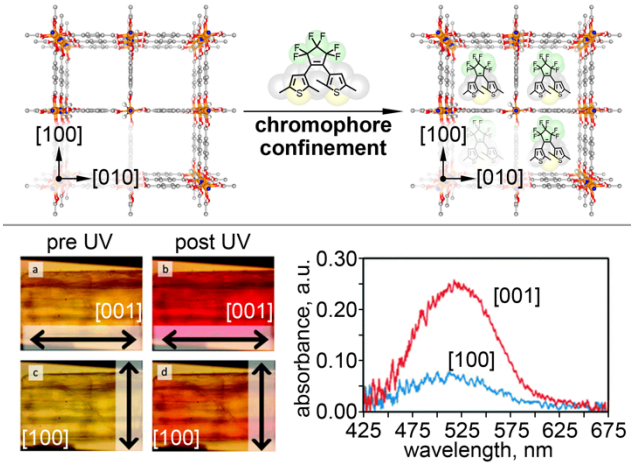

Fig. 6 (*top*) Schematic representation of confinement-driven linear dichroism in 1,2-bis(2,5-dimethyl-thien-3-yl)perfluorocyclopentene@$Zn_2(BDC)_2(DABCO)$ single crystals. (*bottom left*) Polarized light images of the single crystals before and after UV irradiation. (*bottom right*) Polarized absorption spectra of a photoresponsive single crystal as a function of single crystal orientation. The orange, green, yellow, gray, blue, and red spheres represent Zn, F, S, C, N, and O atoms, respectively. H atoms were omitted for clarity. Reproduced from ref. 89 with permission from American Chemical Society, copyright 2016.

benzenedicarboxylic acid; DABCO = 1,4-diazabicyclo[2.2.2]octane), the crystals turned dark red and exhibited strong linear dichroism. Moreover, the diarylethene guest molecules were preferentially aligned within the pores of the host along the crystallographic *c*-axis.

Currently, COFs are also actively explored as a platform for photochromic guest immobilization. Very recently, the electronic properties of a COF were tuned through incorporation of SP as a function of light.[90] In this case, the COF provided sufficient void space for SP structural rearrangement associated with its photoisomerization. Upon UV-irradiation, the spiropyran derivative isomerized to the charge-separated merocyanine form within the COF, resulting in a nearly 40% increase in conductivity compared to that of SP@COF before UV-irradiation.

2.3 Transition Metal Polyimine Guests

Transition metal complexes are another important class of molecules for incorporation into porous motifs such as MOFs (Fig. 7). Complexes including polyoxometalates, metalloporphyrins, metal polyimines, and phthalocyanines exhibit photophysical properties that are important for light-harvesting applications and photocatalysis including broad wavelength absorption, long-lived excited states, and relatively high photostability.[71,72,91,92] In addition, derivatives of transition metal complexes have been integrated into MOFs as a part of the framework backbone and produced intriguing photophysical properties.[70,73] The photophysical properties of transition metal complexes arise from the *d* orbital occupancy as well as the electronic structure of the coordinated ligands,

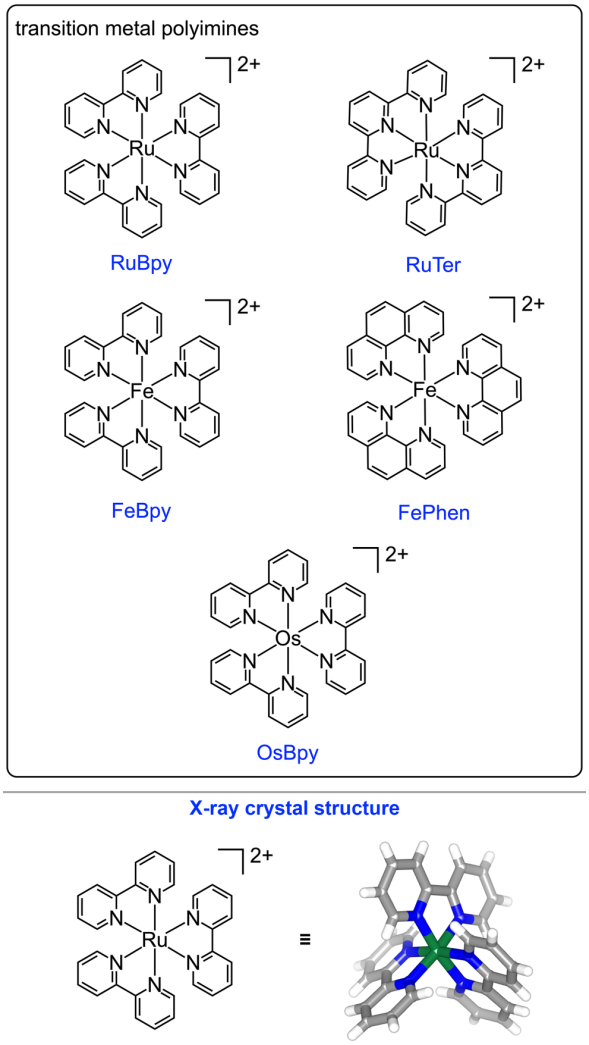

Fig. 7 (*top*) Structures of transition metal polyimines encapsulated in MOFs and discussed in this review. (*bottom*) The Ru(II) tris(2,2'-bipyridine) dication. The green, gray, blue, and white colors represent Ru, C, N, and H atoms, respectively.

and can be significantly influenced by confinement within porous materials.

2.3.1 Transition Metal Polyimine Photophysics

One of the most well studied classes of transition metal complexes contain polyimine ligands such as 2,2'-bipyridine (Bpy), 1,10-phenanthroline (Phen), and 2,2',6,2"-terpyridine (Ter), and are coordinated to group 8 transition metals such as Fe(II), Ru(II), and Os(II) (Fig. 7).[93–99] Of these complexes, ruthenium (II) tris-(2,2-bipyridine) (RuBpy) is the most well-understood regarding electronic structure and photophysical properties and serves as a model for other transition metal polyimines (Fig. 7).[100] Excitation of RuBpy results in an electronic transition from the t_{2g} orbital of Ru(II) to the anti-bonding π^* orbital of the coordinated Bpy ligand, producing a singlet metal-to-ligand charge transfer (^{1}MLCT) excited state. The ^{1}MLCT

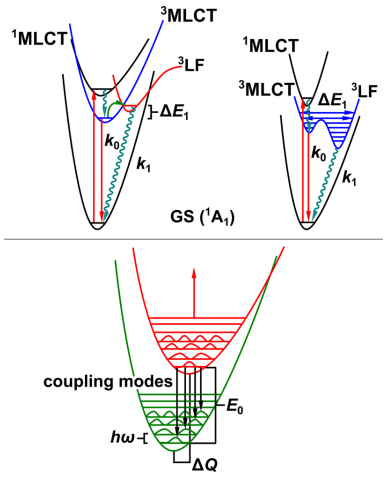

Fig. 8 (*top*) Schematic representation of the potential energy surfaces for RuBpy in the (*left*) weak and (*right*) strong coupling limit between the excited ^{3}MLCT and ^{3}LF states. (*bottom*) Diagram illustrating the kinetic parameters described in eqn (2) and (3).

decays (~5–15 ps) to a set of three closely spaced ^{3}MLCT states that can decay either radiatively (k_r) or non-radiatively (k_{nr}) to the singlet ground state (^{1}GS; Fig. 8).[100] In addition, a thermally accessible triplet ligand field state (^{3}LF) can be populated that decays through a non-radiative (k_1) pathway back to the ^{1}GS. The conversion from the ^{3}MLCT to the ^{1}GS is a spin-forbidden process, resulting in a long-lived excited state with a lifetime on the order of 600 ns.

The excited state decay pathways summarized in Fig. 8 can be described using a transition state theory formalism according to eqn (1):[93]

$$\frac{1}{\tau_{obs}} = k_{obs} = k_0 + k_1 \times e^{\left(\frac{-\Delta E}{k_b T}\right)} \qquad (1)$$

where k_b is the Boltzmann's constant, ΔE is the energy barrier to access excited states above the lowest energy emitting states, k_1 is the rate constant associated with decay from the higher energy state, and k_0 is the sum of the non-radiative and radiative decay from the lowest energy emitting state. For RuBpy in ethanol, k_0 is 6.0×10^5 s^{-1}, k_1 is 1.9×10^{13} s^{-1}, and ΔE is 3491 cm^{-1}; ΔE is related to thermal access to the higher energy ligand field state, ^{3}LF.[101] The ^{3}LF state is anti-bonding with respect to the Ru–ligand bond, and the ΔE for Ru(II) type complexes can vary depending on the nature of the coordinated ligands. For example, Ru(II) coordinated with bis-(2,2',6,2"-terpyridine) (RuTer) coordination exhibits a significantly lower barrier (~1500 cm^{-1}) resulting in a much shorter emission lifetime (τ < 1 ns) and a low luminescence QY (Φ < 1%), relative to RuBpy. For transition metal polyimine systems such as Fe(II) tris(2,2'-bipyridine) (FeBpy), the ^{3}LF state is lower in energy than the ^{3}MLCT state and deactivates through conversion to a lower energy ^{5}LF excited state. In the case of Fe(II) complexes such as

FeBpy and Fe(II) tris-(1,10-phenanthroline) (FePhen), rapid decay from the ^{5}LF state gives rise to lifetimes of < 1 ns and low luminescence QYs, Φ < 0.1%. In order to understand the effects of confinement on the excited state decay pathways, a Frank-Condon analysis of the steady-state emission spectra can be applied using eqn (2):

$$I(E) = \Sigma_{n=0}{}^{N}\Sigma_{m=0}{}^{M}\left[\frac{(E_{00} - nh\omega_H - mh\omega_L)}{E_{00}}\right]^4 \left(e^{\frac{-S_H}{n!}}\right)\left(e^{\frac{-S_L}{m!}}\right)$$

$$\text{Exp}\left[-4\ln 2\,(\tfrac{E-E_{00}+nh\omega_H+mh\omega_L}{\Delta\nu_{\frac{1}{2}}})^2\right] \qquad (2)$$

where $I(E)$ is the emission intensity at energy E, E_{00} is the energy gap between the excited and ground state zero point energies, $h\omega_H$ and $h\omega_L$ are the average high and low frequency acceptor modes, respectively, S_H and S_L are the vibronic coupling factors (Huang-Rhys factors), $\Delta\nu_{1/2}$ is the full width at half maximum, and n and m are the high and low frequency vibrational quantum numbers, respectively. In the case of Bpy- and Phen-containing transition metal complexes, the average high frequency acceptor modes are between 1000–1500 cm^{-1} and the average low frequency modes are between 200–700 cm^{-1}. The Huang-Rhys factor (S_i) and the average frequencies of the coupling modes ($h\omega_i$) are related to changes in the overall potential energy surfaces that accompany changes in geometry (ΔQ) through eqn (3):

$$S_i = M(\tfrac{1}{2})(\tfrac{h\omega_i}{\hbar})(\Delta Q)^2 \qquad (3)$$

where $\hbar$ is the reduced Planck's constant and M is the reduced mass of the vibrating system (Fig. 8).

2.3.2 Ru(II) polyimine@Zn-Polyhedral MOFs

Metal-organic frameworks composed of zinc (II) ions and carboxylate-based ligands are some of the earliest examples of MOFs with high porosity and large surface areas.[102–105] A prototypical polyhedral Zn(II)-carboxylate MOF is $Zn_3(BTC)_2$ (Fig. 9).[106] The $Zn_3(BTC)_2$ MOF forms three distinct cavity structures: a smaller tetrahedron cavity (~5 Å in diameter), an ~11 Å octahemioctahedron, and a ~13 Å rhombihexahedron.[107] The USF-2 framework, developed by Larsen and coworkers, is shown in Fig. 9. USF-2 is also formed from Zn(II) ions and BTC^{3-} ligands, is isostructural to $Zn_3(BTC)_2$, and contains three cavity sizes similar to those in $Zn_3(BTC)_2$ including a ~9 Å cuboctahedral cage, a ~13 Å octahemioctahedral cage, and a ~15 Å rhombicuboctahedral cage.[108] The diameter of RuBpy is ~11 Å, and therefore, can be accommodated within the ~13 Å rhombihexahedron cage of USF-2 or in the case of $Zn_3(BTC)_2$, the ~13 Å octahemioctahedral cage or the ~15 Å rhombicuboctahedral of (Fig. 9).

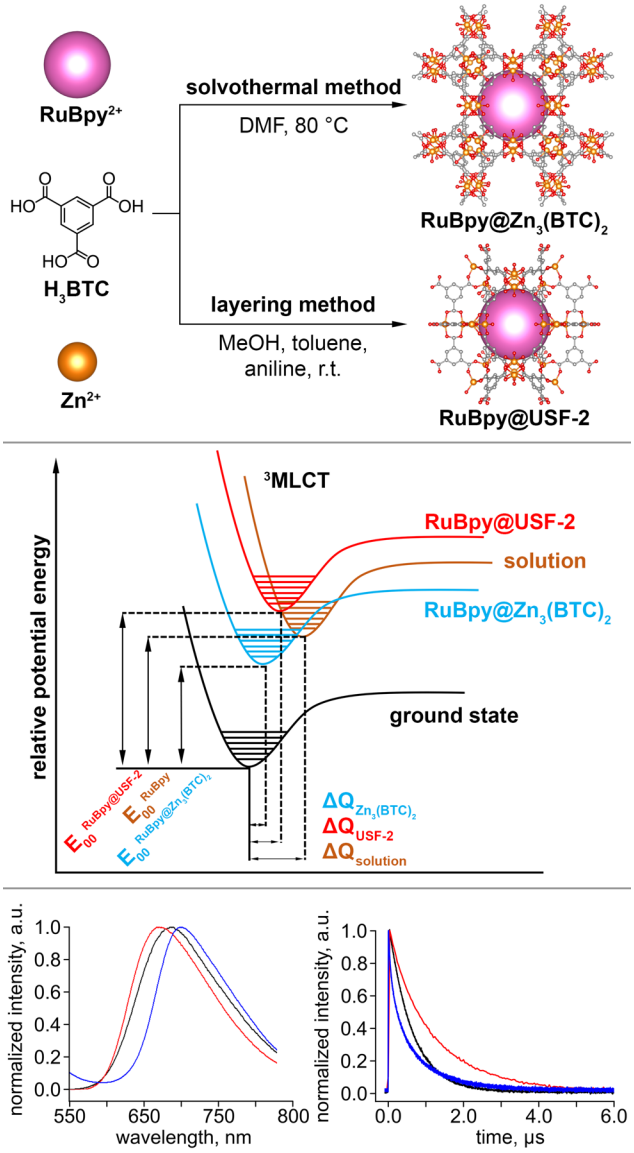

Fig. 9 (*top*) Synthesis of RuBpy@$Zn_3(BTC)_2$ and RuBpy@USF-2. Reproduced from ref. 106 with permission from Elsevier, copyright 2018. (*middle*) Diagram illustrating the displacement of the excited state potential surfaces of RuBpy@USF-2 and RuBpy@$Zn_3(BTC)_2$, relative toc RuBpy in solution. Reproduced from ref. 109 with permission from Springer Nature, copyright 2020. (*bottom left*) Steady-state emission spectra of RuBpy in EtOH (black), RuBpy@USF-2 (red), and RuBpy@$Zn_3(BTC)_2$ (blue). (*bottom right*) The emission decays for RuBpy in EtOH (black), RuBpy@USF-2 (red), and RuBpy@$Zn_3(BTC)_2$ (blue). The orange, gray, and red spheres represent Zn, C, and O atoms, respectively. H atoms were omitted for clarity. Reproduced from ref. 108 with permission from American Chemical Society, copyright 2012.

The effect of encapsulation on the photophysics of RuBpy is evident from the steady-state emission spectra (Fig. 9) and is dependent upon the nature of the framework.[106] The steady-state emission spectra of RuBpy@USF-2 is hypsochromically shifted relative to that of RuBpy in solution, that is consistent with a destabilization of the lowest energy emitting ^{3}MLCT, possibly due to the interaction between the excited state dipole moment and the overall charge associated with the cavities.[108]

Table 1: Summary of Franck-Condon parameters for transition metal polyimines and their incorporation into MOFs.[106,108,111–114]

species	E_{00} (cm^{-1})	$h\omega_H$; $h\omega_L$ (cm^{-1})	S_H; S_L	$\Delta\nu_{1/2}$ (cm^{-1})	cavity shape; size (Å)
RuBpy in EtOH	16781	1258; 355	0.64; 0.73	1617	N/A
RuBpy@ USF-2	16814	1257; 129	0.65; 0.10	1561	rhombi cuboctahedral; 15
RuBpy@ $Zn_3(BTC)_2$	16359	1207; 279	0.60; 0.10	1511	rhombi hexahedron; 13
RWLC-1	17364	1589; 463	0.62; 0.68	1726	hexagonal; 14
RWLC-2	16213	1918; 347	0.55; 0.73	2668	cubic; 14
RWLC-3	16524	2471; 846	0.14; 0.19	1076	cubic; 13
RWLC-5	15915	1738; 636	0.31; 0.10	1463	cubic; 13
RWLC-6	16927	1257; 391	0.67; 0.68	1396	hexagonal; 15
RuBpy@ UiO-66	16651	1387; 304	0.63; 0.71	1640	octahedral; 12
OsBpy in EtOH	14163	1486; 558	0.30; 0.55	1227	N/A
OsBpy@ USF-2	14258	1174; 353	0.35; 0.67	949	rhombi cuboctahedral; 15
OsBpy@ $Zn_3(BTC)_2$	14274	1057; 276	0.47; 0.67	1207	rhombi hexahedron; 13

In the case of USF-2, the framework is composed of cationic cavities that may play a role in the polarization of the large excited state dipole moment of RuBpy (~4.6 D) that destabilizes the ^{3}MLCT.[110] A Frank-Condon analysis of the RuBpy@USF-2 emission spectrum revealed changes in the average low frequency acceptor mode and low coupling factor (S_L), indicating partial distortion of the complex upon encapsulation (Table 1). The extent of the distortion can be obtained from the $\Delta Q_{MOF}/\Delta Q_{soln}$ ratio given in eqn (4):

$$\frac{\Delta Q_{MOF}}{\Delta Q_{soln}} = \left(\frac{S^{MOF}\hbar\omega^{soln}}{S^{soln}\hbar\omega^{MOF}}\right)^{\frac{1}{2}} \qquad (4)$$

The ratio $\Delta Q_{MOF}/\Delta Q_{soln}$ for RuBpy@USF-2 is ~0.81 indicating a small perturbation in the RuBpy excited state potential surface in the MOF relative to solution.

The emission decay data (Fig. 9) for RuBpy@USF-2 can be fit to a single exponential decay function revealing an excited state lifetime twice that observed for RuBpy in solution (1200 ns for RuBpy@USF-2 vs. 614 ns for RuBpy in ethanol).[106] In addition, no changes were observed for the decay of the lowest energy ^{3}MLCT manifold (k_0 in eqn (1) and Table 2) while the non-radiative decay term for the ^{3}LF decay (k_1 in eqn (1)) increased by a factor of ~30 relative to solution. The ΔE also increased by~930 cm^{-1} upon encapsulation, indicating a rise in the energy barrier to access the ^{3}LF state above the emissive ^{3}MLCT state.

Table 2: Summary of the kinetic parameters for transition metal polyimines and their incorporation into MOFs.[98,106,108,111–113]

species	k_0 (s^{-1}) × 10^6	k_1 (s^{-1}) × 10^{13}	ΔE_1 (cm^{-1})	τ (ns)[a]	cavity shape; size (Å)
RuBpy in EtOH	5.6	5.1	3661	614	N/A
RuBpy@ USF-2	5.5	150	4593	1200	rhombi cuboctahedral; 15
RuBpy@ $Zn_3(BTC)_2$	7.2	0.14	3033	744	rhombi hexahedron; 13
RWLC-1	5.3	0.002	2566	1600	hexagonal; 14
RWLC-2	7.6	0.002	2198	797	cubic; 14
RWLC-3	3	0.001	1779	453	cubic; 13
RWLC-5	--	--	--	1167	cubic; 13
RWLC-6	5.5	0.2	3084	1032	hexagonal; 15
RuBpy@ UiO-66	9.0	0.05	2986	1004	octahedral; 12
OsBpy in EtOH	10	0.00006	975	50	N/A
OsBpy@ USF-2	9.0	0.0002	1313	81	rhombi cuboctahedral; 15
OsBpy@ $Zn_3(BTC)_2$	7.0	0.0001	1252	104	rhombi hexahedron; 13

[a]The slow phase component of all lifetimes was obtained from fits of the lifetime decays to eqn (1).

As the ^{3}LF state involves increased Ru–N bond lengths, confinement restricts the expansion of the complex, thereby raising ΔE and reducing the ^{3}LF state population. As the ^{3}LF state decays via a large non-radiative rate constant and the populations reduce, an increased emission lifetime was observed (Table 2).

A comparison of the steady-state emission spectra and lifetime decay of RuBpy@$Zn_3(BTC)_2$ and RuBpy@USF-2 indicated that the nature of the cavities within the Zn(II) framework plays an important role in modulating the photophysics of the RuBpy complex.[106] The steady-state emission spectra of RuBpy@$Zn_3(BTC)_2$ (Fig. 9) displayed a bathochromic shift relative to RuBpy in solution, contrasting to RuBpy@USF-2, and is consistent with stabilization of the ^{3}MLCT in $Zn_3(BTC)_2$. Since $Zn_3(BTC)_2$ lacks the periodic interconnecting $[Zn_2(COO^-)_3]^+$ clusters, formation of the excited state dipole moment likely induced polarization within the cavity that further stabilized the ^{3}MLCT state. A Frank-Condon analysis of the RuBpy@$Zn_3(BTC)_2$ emission spectra revealed changes to the

Huang-Rhys low frequency coupling factor (S_L) by nearly 86% relative to solution.

As observed in RuBpy@USF-2, encapsulation of RuBpy also induced geometric distortion of the complex that decreased the low frequency coupling factor and changed the average low frequency acceptor modes. The calculated ratio of $\Delta Q_{MOF}/\Delta Q_{soln}$ for RuBpy@$Zn_3(BTC)_2$ was found to be ~0.70 indicating perturbation to the potential energy surface of the complex upon encapsulation, similar to RuBpy@USF-2. Unlike RuBpy@USF-2, the emission decay of RuBpy@$Zn_3(BTC)_2$ fit best to a biphasic decay function, indicating two populations of RuBpy. The slower decay phase exhibited an increased emission lifetime of 744 ns, compared to 614 ns for RuBpy in ethanol, while the faster decaying phase exhibited a lifetime of 133 ns. The slower phase was the result of RuBpy encapsulated in the 11 Å octahemioctahedron, the 13 Å rhombihexahedron cavities, or a combination of the two. The values of k_1 and ΔE decreased relative to RuBpy in solution, while k_0 increased relative to solution (Tables 1 and 2). A decrease in ΔE would suggest a decrease in the emission lifetime rather than the observed increase in lifetime. The fact that the energy barrier to access the ^{3}LF decreased while the observed emission decay lifetime increased suggests that the observed energy barrier is actually to access higher energy ^{3}MLCT states, while the barrier to access the ^{3}LF state was too large to allow for any significant population of this state. This observation further suggested that RuBpy may be encapsulated primarily within the smaller (~11 Å) cavity in $Zn_3(BTC)_2$ that significantly restricted excited state expansion.

2.3.3 Ru(II) polyimine Templated-Frameworks

Templating agents are often used in MOF synthesis to produce new topologies that are either thermodynamically or kinetically inaccessible in the absence of the template.[115–118] One suggestion is that the templating molecule interacts with synthetic intermediates of the MOF through weak forces such as van der Waals interactions, hydrogen bonding, or other electrostatic forces.[115,117,118] Templating molecules can include solvents, organic and inorganic molecules, surfactants, and polymers.[115,117,118] RuBpy and related Ru(II) polyimine complexes are emerging as an important class of transition metal templating agents for the synthesis of photoactive MOFs for light-harvesting and photocatalytic applications.[111,112,118] Recently, the templating effects of RuBpy type complexes have been exploited to produce a number of novel RuBpy-MOFs in which the Ru(II) cation is crystallographically resolved within the frameworks.[113,114] For many of these MOFs, the frameworks do not form in the absence of the Ru(II) complexes.

RWLC-1 and RWLC-2 Frameworks. The first examples of RuBpy templated MOFs were produced by Larsen and coworkers.[111] These frameworks (RWLC-1 and RWLC-2) were synthesized solvothermally from Zn(II) cations and benzene-1,3,5-tribenzoic acid (H_3BTB) in the presence of RuBpy (Fig. 10).[111] The RWLC-2 MOF is structurally similar to MOF-39 with RuBpy encapsulated

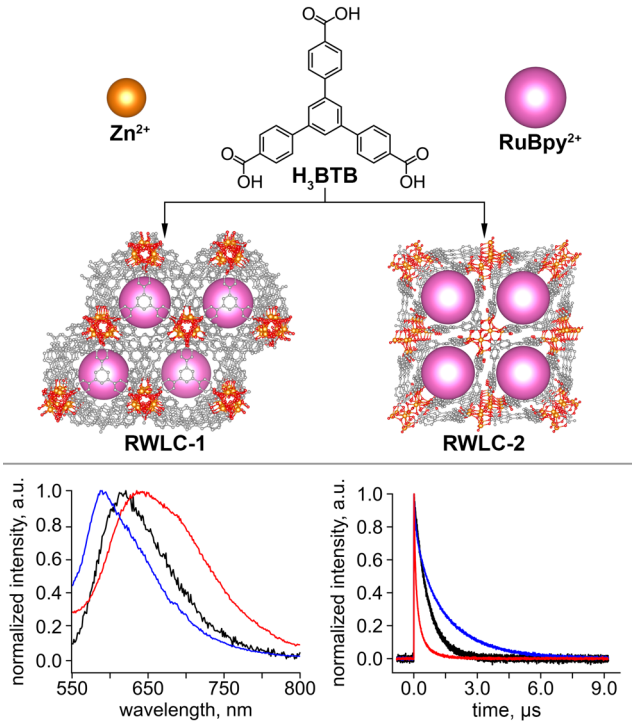

Fig. 10 (*top*) Synthesis of RWLC-1 and RWLC-2 MOFs. (*bottom left*) Steady-state emission spectra of RuBpy in EtOH (black), RWLC-1 (blue), and RWLC- 2 (red). (*bottom right*) The emission decays for RuBpy in EtOH (black), RWLC-1 (blue), and RWLC- 2 (red). The orange, gray, and red spheres represent Zn, C, and O atoms, respectively. H atoms were omitted for clarity. Reproduced from ref. 111 with permission from American Chemical Society, copyright 2014.

in the long channels of the framework (Fig. 10).[119] The steady-state emission spectra of RWLC-1 was hypsochromically shifted relative to RuBpy in solution (583 nm and 614 nm, respectively) while that of RWLC-2 was bathochromically shifted (Fig. 10). Examination of the RWLC-1 crystal structure revealed two RuBpy cations in close proximity with no resolvable solvent molecules, indicating that the tight cavities of the framework likely prevent solvent accessibility to the RuBpy complex. Therefore, solvent reorganization is limited and restricts thermal relaxation of the emitting ^{3}MLCT state. Similar results have been observed for dehydrated RuBpy@ZeoliteY (589 nm for RuBpy@ZeoliteY vs. 626 nm for RuBpy in water).[120] In the case of RWLC-2, the bathochromic shift in the emission band indicated stabilization of the ^{3}MLCT which could arise from increased solvent within the framework, resulting in greater solvent reorganization. As shown in Table 2, the emission fit parameters for both RWLC-1 and RWLC-2 are quite similar to RuBpy in ethanol indicating that confinement of the complex does not distort the excited or ground state potentials significantly. The $\Delta Q_{MOF}/\Delta Q_{soln}$ ratios for RWLC-1 and RWLC-2 are 0.86 and 0.88, respectively, and are consistent with minimal distortion of the complex upon encapsulation in both systems, similar to what is observed for the RuBpy@USF-2 and RuBpy@$Zn_3(BTC)_2$ MOFs.

The emission decays for both RWLC-1 and RWLC-2 were best fit to a biexponential function indicating two populations of RuBpy in both frameworks (Fig. 10).[111] For RWLC-1, the slower phase exhibits an emission lifetime of 1600 ns relative to ~614 ns for RuBpy in solution and a faster phase lifetime of 237 ns. For the corresponding RWLC-2 framework, the slower phase exhibited a lifetime of 797 ns and the fast phase exhibited a lifetime of 171 ns. Interestingly, both ΔE and k_1 decreased for RWLC-1 and RWLC-2, indicating thermal population of a higher energy ^{3}MLCT (Table 2). Larsen and coworkers hypothesize that the population of RuBpy giving rise to the slow phase decay was likely confined within the hexagonal channels of RWLC-1 and the cubic channels of RWLC-2. Since the ΔE term decreased relative to RuBpy in solution, the energy barrier to access the ^{3}LF was sufficiently high as to restrict access altogether as in the case of RuBpy@$Zn_3(BTC)_2$. Thus, a MLCT state that is higher in energy than the fourth MLCT state, including additional singlet-in-character MLCT states, is thermally accessible and contributes to the emission decay. The slow phases of RWLC-1 and RWLC-2 were similar to the slow phase of RuBpy@$Zn_3(BTC)_2$ that exhibited a ΔE = 3033 cm^{-1} and a k_1 ~10^{11} s^{-1} while the RuBpy@USF-2 exhibited only slight deactivation of the ^{3}LF state with a ΔE of 3600–4600 cm^{-1} and k_1 on the order of ~10^{13} s^{-1}. For the fast phase component, the k_0 term increased by a factor of ~7 for both RWLC-1 and RWLC-2, while the k_1 and ΔE were similar to solution (Table 2). This is consistent with deactivation of the lowest emitting ^{3}MLCT state associated with surface adsorption of RuBpy during the solvothermal synthesis, resulting in clustering of RuBpy complexes that led to self-quenching.

RWLC-3 Framework. The reaction of H_2BDC and Zn(II) nitrate resulted in the formation of MOF-5, a well-known framework.[121] Interestingly, synthesis in the presence of RuBpy produced a two-fold interpenetrated pillared honeycomb **bbn** network forming, RWLC-3.[112] The negatively charged framework was neutralized by the cationic nature of the encapsulated RuBpy within the channels (Fig. 11).

The steady-state emission spectrum of RWLC-3 revealed a relatively small bathochromic shift relative to RuBpy in solution, that is consistent with a slight decrease in E_{00} (ΔE_{00} = 257 cm^{-1}) extracted from the Frank-Condon fit of the emission data. The Frank-Condon fit parameters also revealed changes in both the average high and low frequency acceptor modes and high and low frequency coupling factors that indicated significant changes in the ^{3}MLCT excited state potential surface of RuBpy in RWLC-3 ($\Delta Q_{MOF}/\Delta Q_{soln}$ ~0.33). The $\Delta Q_{MOF}/\Delta Q_{soln}$ ratio further suggested that confinement may distort the equilibrium ground state complex as well as the excited state ^{3}MLCT state.

As with the RWLC-1 and RWLC-2 templated MOFs, the emission decay of RWLC-3 best fit a biexponential function with a slow phase of 453 ns and a fast phase of 123 ns.[112] The slower phase of RWLC-3 was significantly shorter relative to the other

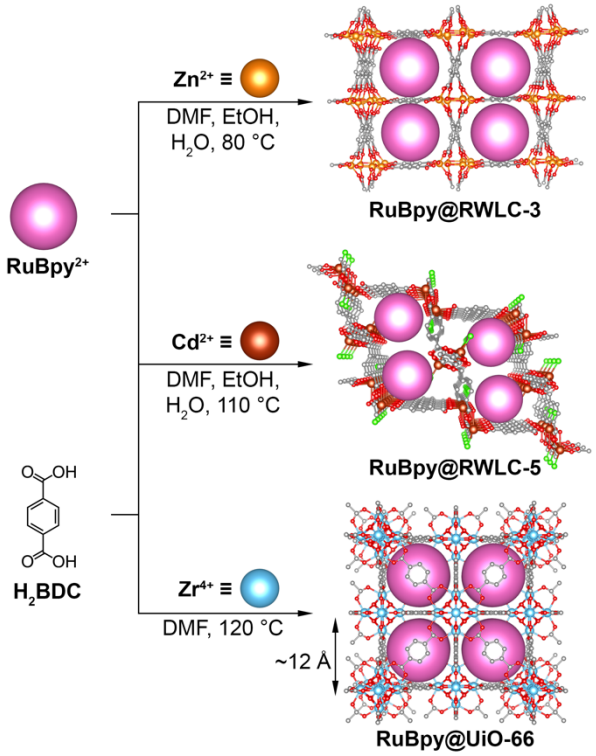

Fig. 11 Synthesis of RuBpy@RWLC-3, RuBpy@RWLC-5, and RuBpy@UiO-66. The orange, bronze, light blue, green, gray, and red spheres represent Zn, Cd, Zr, Cl, C, and O atoms, respectively. H atoms were omitted for clarity. Reproduced from ref. 104 with permission from Royal Society of Chemistry, copyright 2013 and from ref. 101 with permission from Elsevier, copyright 2017.

Zn-templated RWLC series (τ = 1600 ns for RWLC-1 and 797 ns for RWLC-2) but was similar to RuBpy@ZeoliteY (τ = 530 ns).[120] The temperature dependent lifetime for the slower phase is consistent with the energy barrier to access the ^{3}LF state and instead allowed access to higher energy ^{3}MLCT states (ΔE = 1779 cm^{-1}). The fast phase decay of RWLC-3 was similar to RWLC-1 and RWLC-2, where the ΔE and k_1 values were close to values of RuBpy in solution, while the k_0 value increased by ~10 fold. The increase in k_0 was most likely due to the surface adsorption of RuBpy on RWLC-3 leading to self-quenching between nearby RuBpy complexes near the surface. The increase in k_0 is most likely due to the surface adsorption of RuBpy on RWLC-3 leading to self-quenching between nearby RuBpy complexes near the surface.

RWLC-6 Framework. The RWLC-6 framework was prepared solvothermally with Zn(II) ions, 1,3,5-tris-carboxyphenylethynyl benzene (H_3BTE), and RuBpy (Fig. 12).[113] The cavities are 15 Å × 23 Å with a **qom** network and the crystal structure revealed electron density in voids that indicate disordered solvent molecules.

The steady-state emission spectrum of RWLC-6 exhibited a hypsochromic shift in the emission band relative to RuBpy in solution that is consistent with confinement of RuBpy in a restricted solvent environment, similar to RWLC-2, RWLC-3, and

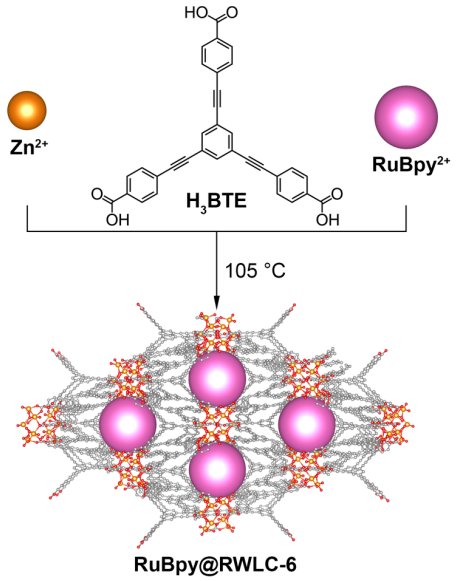

Fig. 12 Synthesis of RuBpy@RWLC-6. The orange, gray, and red spheres represent Zn, C, and O atoms, respectively. H atoms were omitted for clarity. Reproduced from ref. 113 with permission from Elsevier, copyright 2019.

RuBpy@$Zn_3(BTC)_2$. A Frank-Condon analysis revealed an increase in E_{00} for RWLC-6, relative to RuBpy in solution, by ~150 cm^{-1} that likely accounts for the slight shift in the emission spectra (Table 1). Solvent inaccessibility to RuBpy would limit the solvent reorganization and prevent thermal relaxation of the emitting ^{3}MLCT state, thus raising the energy. The average high and low frequency modes are only slightly altered relative to solution with the Huang-Rhys low frequency coupling factor being the most affected. The ratio of $\Delta Q_{MOF}/\Delta Q_{soln}$ for RWLC-6 is ~0.97 indicating essentially no structural perturbations upon encapsulation.

Following the trends observed for other members of the RWLC series of MOFs, the emission decay of RWLC-6 was biphasic with a slow phase lifetime of 1032 ns and a fast phase lifetime of 216 ns. Interestingly, the ΔE and k_1 terms were quite distinct from the other RWLC MOFs, more closely resembling RuBpy@USF-2 and RuBpy@$Zn_3(BTC)_2$ (ΔE = 3084 cm^{-1} and k_1 = 2.3 × 10^{12} s^{-1}), while k_0 remained unchanged relative to RuBpy in solution (Table 2). The decrease in k_1 indicated non-radiative decay from a state other than the ^{3}LF with ΔE being a barrier to thermal population of a higher energy ^{3}MLCT state. The fast phase decay kinetics revealed a large decrease in both ΔE and k_1 values and an increase in k_0. The k_1 value decreased by a factor of ~106 and the ΔE decreased by over 3000 cm^{-1}, indicating that the RuBpy population, giving rise to the fast phase, was also located in a confined environment and likely restricted the complex enough to prohibit access to the ^{3}LF state (Table 1, Fig. 13). The large increase in k_0 further indicates an increase in either the non-radiative or radiative components of the emitting ^{3}MLCT or the presence of an undefined quenching mechanism. As observed in RuBpy@$Zn_3(BTC)_2$,

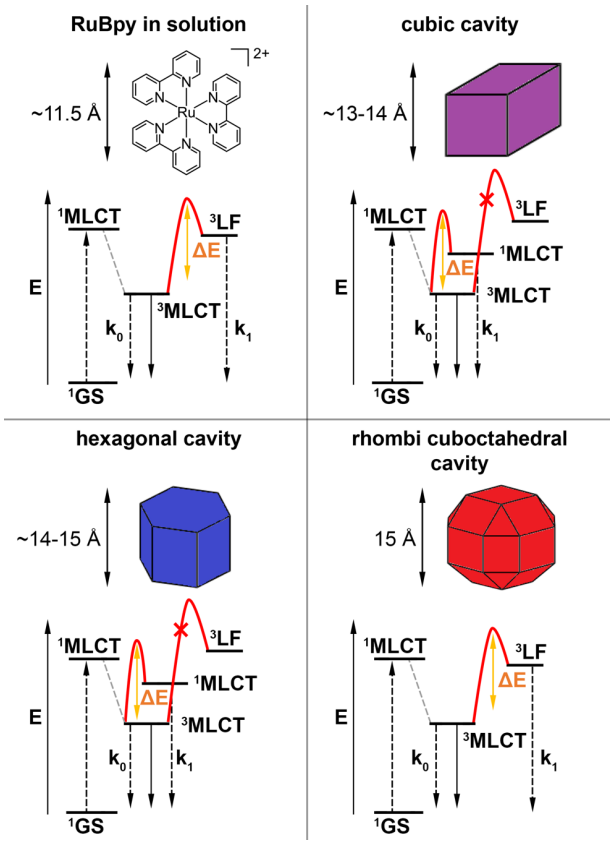

Fig. 13 Illustration of the effects of encapsulation on the energy levels of RuBpy as a function of cavity diameter and geometry. Reproduced from ref. 96 with permission from Elsevier, copyright 2019, ref. 111 with permission from American Chemical Society, copyright 2013, and ref. 108 with permission from American Chemical Society, copyright 2012.

RWLC-1, and RWLC-2, the fast phase was most likely due to closely spaced RuBpy complexes that participated in a self-quenching process.

Cd^{2+} based RWLC-5 Framework. The RWLC-5 framework resulted from the synthesis of RWLC-3 in the presence of Cd^{2+} instead of Zn^{2+} (Fig. 11).[114] A characteristic of this framework is the presence of channels with RuBpy cations forming π–π interactions (between other RuBpy cations) and π–CH interactions (between RuBpy cations and BDC^{2-} ligands). The crystal structure also revealed the presence of disordered water molecules (~34%) in sites that hydrogen bond with the carboxylates and RuBpy cations.

The RWLC-5 framework displayed many features similar to the Zn-RWLC series, such as a bathochromically shifted emission spectrum, changes in both the high and low average frequency acceptor modes and the high and low frequency coupling factors, in comparison to RuBpy in solution (Table 1). Interestingly the $\Delta Q_{MOF}/\Delta Q_{soln}$ for RWLC-5 is similar to that of RWLC-3 (0.43 versus 0.33 for RWLC-3) and much lower than the other RuBpy encapsulated MOFs, indicating a relatively large distortion of the complex upon encapsulation. The emission

lifetime data for RWLC-5 was best fit to a biexponential decay with a slower lifetime of 1167 ns and a faster lifetime of 126 ns. The lifetime data for both the slower and fast phases of RWLC-5 displayed no temperature dependence that indicates there were not any thermally accessible states above the emissive ^{3}MLCT state. Interestingly, the population percentage of the fast phase was nearly equivalent to the 34% of disordered water molecules within RWLC-5, suggesting that there are sites within hydrogen bonding distance of the RuBpy complex. Hydrogen bonding interactions between the water cluster and the 2,2'-biyridines of RuBpy likely resulted in the non-radiative decay of the emissive ^{3}MLCT manifold.

Ru(II) polyimine@Zr-MOFs. The use of Zr(IV) together with carboxylate based linkers has led to the development of MOFs with large surface areas, inherent catalytic abilities, and exceptional stability, particularly with regards to aqueous environments.[122,123] One of the most widely examined classes of Zr(IV)-based MOFs is the UiO series (UiO = University of Oslo).[122,124,125] In particular, UiO-66 exhibits two cavity geometries, the first being tetrahedral with a diameter of ~7.5 Å and the second being octahedral with a diameter of ~12 Å. As an important consideration, the larger cavity is of appropriate dimension for the encapsulation of transition metal polyimine guests (Fig. 13).[96] One of the first examples of non-covalent Ru(II) polyimine encapsulation into a Zr(IV)-framework is RuBpy@UiO-66.[96,101] As observed for most non-covalent encapsulation of RuBpy, the RuBpy@UiO-66 exhibited changes in photophysical properties relative to RuBpy in solution. The steady-state emission spectrum revealed a slight bathochromic shift of the emission band relative to RuBpy in solution (615 nm for RuBpy@UiO-66 vs. 608 nm for RuBpy in ethanol) similar to RWLC-2, RWLC-3 and RWLC-5.[96] A bathochromic shift of the emission band most likely arises from a stabilization of the emissive ^{3}MLCT state due to the electrostatic interactions within the UiO-66 cavities. Moreover, the SBUs are inherently anionic due to the hydroxide ligand that could participate in the stabilization of the large excited state dipole moment of RuBpy. Neither the average high and low frequency acceptor modes or the high and low coupling factors (S_H and S_L) change relative to solution, indicating negligible geometric distortion of the complex upon encapsulation. This is further supported by the average ratio (high and low frequency and coupling factors, Table 1) of $\Delta Q_{MOF}/\Delta Q_{soln}$ for RuBpy@UiO-66 which is ~1.

The emission lifetime data of RuBpy@UiO-66 fit a biexponential decay function with a longer phase lifetime of 1004 ns and shorter phase lifetime of 187 ns, similar to the other MOFs described above.[96] The slow phase component of RuBpy@UiO-66 exhibited a 227-fold decrease in k_1 and ~500 cm^{-1} decrease in the ΔE term while the k_0 term slightly increased relative to RuBpy in solution (Table 2).[96] The decrease in both the energy barrier and k_1 are consistent with a complete deactivation of the higher energy ^{3}LF state and thermal population to one of the higher in energy singlet-in-character MLCT state. The fast phase emission decay exhibited an increase in all three parameters: k_1, k_0, and ΔE. Likely the population giving rise to the fast phase was still thermally populating the ^{3}LF state with a large ~10 fold increase in k_0, attributed to surface absorption of closely spaced RuBpy complexes resulting in self-quenching.

Another approach to unite Ru(II) polyimines and Zr(IV)-based MOFs is through the strategic design of Ru(II) polyimine linkers for coordinative immobilization. For example, Morris and coworkers utilized a combination of Ru(II) bis-(2,2'-bipyridine)(2,2'-bipyridine-5,5'-dicarboxylic acid) (RuDCBPY) and H_2BPDC (H_2BPDC = [1,1'-biphenyl]-4,4'-dicarboxylic acid) to grow a series of RuDCBPY-UiO-67 thin films.[73] Investigation of their thin films as photosensitizers for photovoltaic applications revealed power conversion efficiencies (PCE) of less than 1%. Although they possessed a low PCE, the MOF sensitized solar cells outperformed a monolayer of the same dye (RuDCBPY) on the surface of TiO_2.[73] These results showcase MOFs as a versatile platform for photovoltaic applications.[126]

2.3.4 Os(II) polyimine Templated-Frameworks

Os(II) tris(2,2'-bipyridine) (OsBpy) is a group (VIII) transition metal complex that is isoelectronic with RuBpy and has been utilized in light-harvesting systems.[94,95] OsBpy displays absorption across a wide range of the visible region with bands

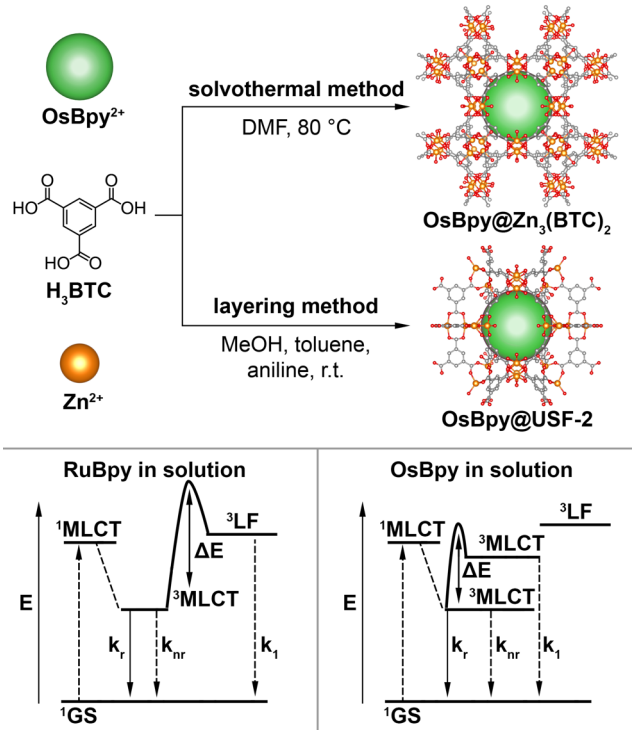

Fig. 14 (*top*) Synthesis of OsBpy@Zn$_3$(BTC)$_2$ and OsBpy@USF-2. (*bottom*) Comparison of the energy level diagrams for RuBpy and OsBpy in solution. The orange, gray, and red spheres represent Zn, C, and O atoms, respectively. H atoms were omitted for clarity. Reproduced from ref. 98 with permission from American Chemical Society, copyright 2020.

centered at 454 nm, 578 nm, 649 nm, and 671 nm with the lowest energy bands (649 nm and 671 nm) attributed to direct excitation from the ^{1}GS to two manifolds of the ^{3}MLCT states due to enhanced spin-orbit coupling.[95] The high energy bands (454 nm and 578 nm) arise from transitions to two manifolds of ^{1}MLCT states. Similar to the RuBpy complex, the excited ^{1}MLCT states decay through intersystem crossing to an emitting ^{3}MLCT manifold with near unity QY. The lowest energy ^{3}MLCT state decays with an observed lifetime (~50 ns) much faster than the RuBpy complex (~620 ns). The excited state decay pathway was also somewhat distinct from that of RuBpy (Fig. 13). Both RuBpy and OsBpy undergo excitation from a singlet ground state to a ^{1}MLCT state within a few fs. The ^{1}MLCT state converts directly to a lower energy manifold of the ^{3}MLCT states with near unity QY. Unlike for RuBpy, there is no low lying ^{3}LF state that can be thermally occupied. Instead, thermal barriers exist to populate ^{3}MLCT states that are at higher energies than the lowest energy emitting ^{3}MLCT state.

Using synthetic procedures similar to RuBpy@USF-2 and RuBpy@$Zn_3(BTC)_2$, analogous scaffolds containing OsBpy could be formed, OsBpy@USF-2 and OsBpy@$Zn_3(BTC)_2$ (Fig. 14). The steady-state emission spectra revealed a large hypsochromic shift for both OsBpy@USF-2 and OsBpy@$Zn_3(BTC)_2$ relative to OsBpy in solution (714 nm for OsBpy@USF-2 and 709 nm for OsBpy@$Zn_3(BTC)_2$ versus 724 nm for OsBpy in methanol).[98] This indicates destabilization of the emissive ^{3}MLCT state which, again, may arise from inefficient solvent reorganization within the MOF similar to several of the RuBpy MOF systems discussed above. Destabilization of the emissive ^{3}MLCT state is supported by a decrease in the E_{00} value for both OsBpy@USF-2 and OsBpy@$Zn_3(BTC)_2$ (Table 1). Like RuBpy, OsBpy exhibits a large excited state dipole moment (~4.87 D) that is strongly affected by the solvent environment.[127] Reducing solvent exposure of OsBpy would increase the energy of the ^{3}MLCT resulting in a hypsochromic shift and increase in E_{00} for both OsBpy@USF-2 and OsBpy@$Zn_3(BTC)_2$. The hypsochromic shift for OsBpy in both USF-2 and $Zn_3(BTC)_2$ is distinct from RuBpy@USF-2 and RuBpy@$Zn_3(BTC)_2$ systems that showed either hypsochromic or bathochromic shifts depending upon MOF cavity charge. OsBpy exhibited similar average low frequency acceptor modes and average high frequency acceptor modes of bipyridine stretching in Ru(II) complexes. Encapsulation shifts the low frequency coupling factors indicating distortion of the complex upon encapsulation (Table 1). This is consistent with the $\Delta Q_{MOF}/\Delta Q_{soln}$ for OsBpy@USF-2 being ~1.3 and for OsBpy@$Zn_3(BTC)_2$ nearly 1.5, indicating significant distortions between the ground and excited states for both systems. The emission lifetime data for both OsBpy@USF-2 and OsBpy@$Zn_3(BTC)_2$ best fit a single exponential function indicating a single population of OsBpy in both systems. For OsBpy@USF-2, the emission lifetime increased relative to OsBpy in solution (80 ns for OsBpy@USF-2 versus 50 ns for OsBpy in methanol) while the emission lifetime of OsBpy@$Zn_3(BTC)_2$ was even longer relative to OsBpy in solution (104 ns OsBpy@$Zn_3(BTC)_2$ versus 50 ns OsBpy in methanol). Temperature dependent lifetime data revealed changes in all three terms for OsBpy@USF-2 and OsBpy@$Zn_3(BTC)_2$ (Table 2). For OsBpy@USF-2, k_1 and ΔE both increased relative to solution, while k_0 decreased slightly. In Os(II) polyimine systems, splitting between the t_{2g} orbitals of the Os(II) ion and the anti-bonding, e_g^*, state was very large. For these complexes, the ^{3}LF state that participated in the non-radiative decay of Ru(II) complexes was not populated in the Os(II) complexes. Rather, several excited states of OsBpy were electronically mixed between ^{3}LF and ^{3}MLCT states. ΔE for OsBpy is associated with the thermal population of a higher energy manifold of three states, $^3A_2$, ^3E, and $^3A_1$ under D_3 symmetry. Radiative decay from a lower energy $^3A_1$ is evident by a low k_0 which is on the order of 106 s^{-1} giving a k_1/k_0 ratio of ~60. In the OsBpy@USF-2 system, the ratio of k_1/k_0 increased by ~220, relative to solution, due to an increase in k_1. The increase in lifetime of OsBpy@USF-2 is thus attributed to the increase in ΔE to access the higher energy ^{3}MLCT* state. Similar changes in the average low frequency acceptor mode and associated coupling factor were observed for OsBpy@$Zn_3(BTC)_2$ concluding similar alteration of the ^{3}LF–^{3}MLCT mixing that enhanced the lifetime.[128]

2.4 Prevention Aggregation of Chromophore Guests through their Spatial Separation inside a Framework

The molecular aggregation of organic fluorescent dye molecules in the solid state, resulting in fluorescence quenching through exciton coupling, i.e., ACQ, is a major challenge that needs to be addressed for their application as solid-state fluorescent materials. ACQ of emission can be diminished by increasing spatial separation of chromophores in dilute solutions; however, this limits their practicability by restricting them to only solution-based applications.[129–131] As a resolution to this phenomenon and opening an avenue for solid-state applications, chromophore separation can be achieved by their inclusion inside discrete framework pores (e.g., MOFs and COFs, Fig. 15). Alignment of chromophores in MOF or COF scaffolds can prevent π–π stacking, and thus, ACQ of emission, result in photoluminescent solid-state materials (Fig. 15). In this section, we will highlight recent progress on strategies used to overcome the ACQ effect by using a MOF or COF.

One of the main driving forces to prevent ACQ of chromophore photoluminescence response is development of solid-state materials possessing high photoluminescence QYs. Several reports have demonstrated that solid-state fluorescent materials can be achieved through separating chromophores in MOF pores (Fig. 15).[2,132–143] For example, Li and coworkers demonstrated that a high QY can be achieved from yellow-

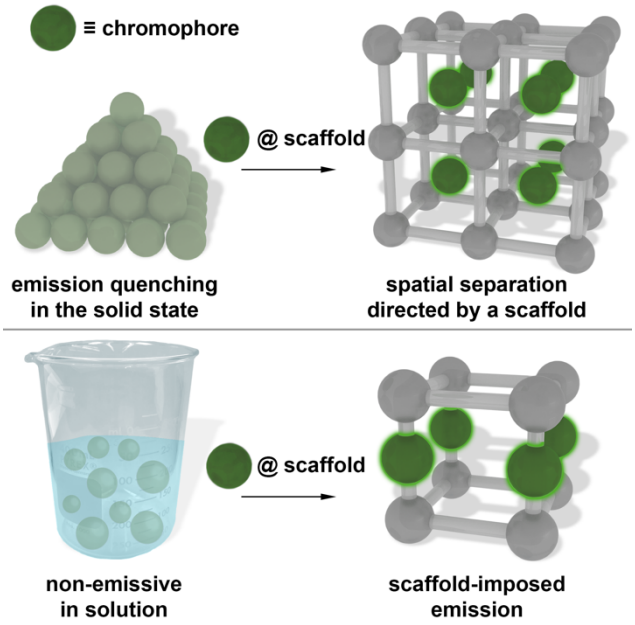

Fig. 15 (*top*) Schematic representation of chromophore aggregation in the solid state and spatial separation of chromophores inside a crystalline scaffold to suppress the ACQ effect. (*bottom*) Schematic representation of emission of chromophores exhibiting AIE behavior by their incorporation into a crystalline scaffold.

emitting dyes such as R6G (R6G = rhodamine 6G; Fig. 16) by their integration into the MOF cavities.[2] In this study, a QY of 63% was measured for R6G@ZIF-8 (ZIF = zeolitic imidazolate framework), portending its potential application as a solid-state yellow phosphor.

The research team of Qian and coworkers demonstrated the advantage of utilizing the organized channels in MOFs to align dyes to promote linearly polarized fluorescence.[77] In this study, induced polarized emission of DASP (DASP = 4-[*p*-(dimethylamino)styryl]-1-methylpyridinium; Fig. 16), a well-known laser dye that exhibits the ACQ effect in the solid state, was observed when it was integrated within the 1D channels of ZJU-68 ($H_2[Zn_3O(CPQC)_3]$; H_2CPQC = 7-(4-carboxyphenyl)quinoline-3-carboxylic acid).

Another study performed by Liu and coworkers demonstrated that a MOF can induce circularly polarized fluorescence of a dye that is confined in MOF pores.[54] In particular, DCM (DCM = 4-(dicyanomethylene)-2-methyl-6-(4-dimethylaminostyryl)-4*H*-pyran; Fig. 16) was integrated in the cavities of a chiral MOF, prepared from Zn^{2+}, 2-methylimidazole, and D- or L-histidine. Besides polarization of the dye's fluorescence response, the emission maximum of DCM is hypsochromically shifted by 62 nm compared to the dye in the solid state. The enhanced fluorescence of the confined chromophore within the MOF was attributed to a suppression of the ACQ effect through increased conformational rigidity of the dye. In fact, the QY increased from 2% for DCM in the solid state to 43% for the DCM@MOF. Furthermore, an increase of

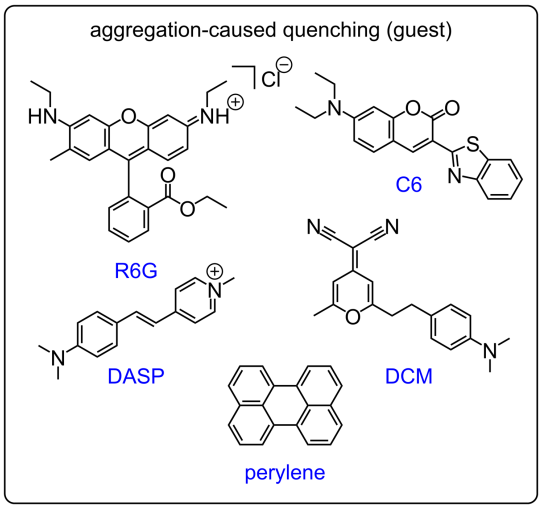

Fig. 16 Structures of guest molecules that typically exhibit ACQ emission in the solid state.

the fluorescence lifetime from 1.8 ns (solid state) to 2.3 ns (DCM@MOF).

Besides suppression of the ACQ effect, confinement of dyes in MOF pores can result in promotion of guest-host ET processes.[20,144] For example, Bu and coworkers demonstrated that ET from a carbazole-based MOF to the dye molecules within the pores could be harnessed for preparation of a white-light-emitting MOF-based luminophore.[20] In this work, DCM and C6, (C6 = 3-(benzo[*d*]thiazol-2-yl)-7-(diethylamino)-2*H*-chromen-2-one; Fig. 16). The crystalline MOF displayed an emission maximum in the blue region at 431 nm upon 371-nm excitation, while the dye encapsulated MOF exhibited emission bands in the blue, green, and red regions corresponding to the parent scaffold, DCM, and C6, respectively. Moreover, by varying the dye concentration in the MOF, the emission profile could be tuned to match the properties of white-light-emitting materials.[20]

In line with these studies, Qian and coworkers demonstrated that ET could occur from an encapsulated dye to the MOF metal node.[144] In this work, perylene (Fig. 16) was embedded in ZJU-88 (Eu_2(QPTCA); H_4QPTCA = 1,1′:4′,1″:4″,1‴-quaterphenyl-3,3‴,5,5‴-tetracarboxylic acid) as a guest, yielding perylene@ZJU-88, that displayed emission bands attributed to perylene and Eu^{3+}. The emission bands assigned to perylene are similar to those exhibited by perylene in DMF rather than that of perylene in the solid state, indicating that the perylene dye molecules encapsulated in the channels of ZJU-88 exhibit behavior of isolated molecules rather than aggregated ones.[144] Moreover, the spectral overlap between perylene emission and Eu^{3+} absorption suggested that ET from perylene to the metal node of the MOF was feasible. Due to the temperature sensitivity of the emission intensity exhibited by perylene-encapsulated MOF, the use of the MOF as a ratiometric thermometer was also demonstrated.[144]

To summarize, the confinement of chromophores in discrete MOF pores has proven to be an effective approach to achieve bright photoluminescence in solid state matrices. As discussed in this section, this approach can not only generate solid state photoluminescent materials, but also allows for remarkable scaffold-imposed photophysical properties (e.g., polarization anisotropy or ET). Although the properties of the chromophores evoked by chromophore confinement in the MOF pores has proven advantageous for a plethora of applications as described in this section, understanding the structure-photophysics relationship is still relatively limited. Therefore, further investigation on this topic is necessary to reveal the full potential of chromophores in solid-state fluorescent materials.

3. Confinement-Driven Linker Photophysics in MOFs and COFs

In addition to guest inclusion inside porous frameworks, coordinative immobilization of chromophores as linkers provides a different pathway to affect the chromophore molecular conformation, and therefore, material photophysics.[145–149] The main advantage of this approach is control over orientation and alignment of chromophores inside a framework that is difficult to achieve in the case of guests. However, a ligand-centered approach for controlling photophysics requires modification of the chromophore core with anchors for engineering of desirable COF or MOF structures. Thus, in this section, we will focus on coordinatively immobilized chromophores.

3.1 BI-based Linkers

Frameworks, in particular MOFs, provide different pathways for chromophore integration through covalent bond formation with the host.[74] Fig. 17 demonstrates chromophore integration: as a part of the scaffold backbone (left), as a side group attached to the linker (middle), or bound directly to the metal nodes (right). In the first case, the framework rigidifies the chromophore due to coordination of both sides of the molecule to metal nodes that can tune the photophysical profile of the embedded chromophore. In the two other cases, pore aperture and geometry may significantly affect chromophore photophysics.

As mentioned in section 2.1, engineering artificial scaffolds that mimic the GFP *β*-barrel behavior is vital for advancing the development of synthetic systems mimicking the photoluminescence behavior of natural proteins. Over the course of several years, Shustova and coworkers were able to gain crucial fundamental understanding of how the confined space of a MOF could simulate the environment of the GFP *β*-barrel by restricting non-radiative decay pathways of BI-chromophores (Fig. 18).[150] Two approaches were utilized to

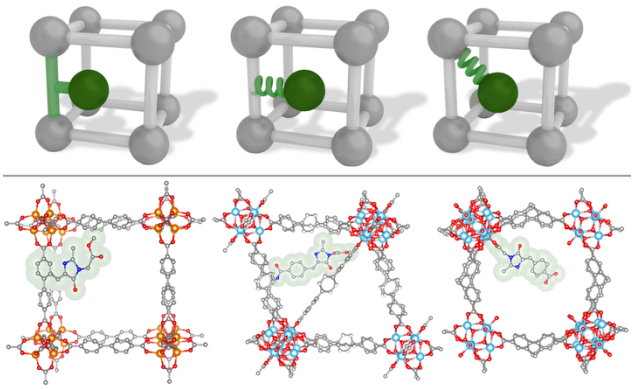

Fig. 17 (*top*) Three strategies for coordinative immobilization of BI-chromophores. (*bottom*) X-ray MOF crystal structure with embedded BI-chromophores.[22,150] The orange, light blue, dark blue, gray, and red spheres represent Zn, Zr, N, C, and O atoms, respectively. H atoms were omitted for clarity.

coordinative immobilize BI-based linkers: integration into crystalline scaffolds through direct synthesis (e.g., $Zr_6O_4(OH)_4(BDC\text{-}BI)_6$ and $Zn_4O(BDC\text{-}BI)_3$; H_2BDC-BI = 2-((1-(2-ethoxy-2-oxoethyl)-2-methyl-5-oxo-1,5-dihydro-4*H*-imidazol-4-ylidene)methyl)-[1,1′-biphenyl]-4,4′-dicarboxylic acid; Fig. 18) and also integration through postsynthetic modification to tether the BI-chromophore as a side group (e.g., $Zn_4O(BDC\text{-}CHO)_{1.1}(BDC\text{-}BI)_{1.9}$; H_2BDC-CHO = 2-formyl-biphenyl-4,4′-dicarboxylic acid).[62,150] The prepared MOFs were able to successfully mimic the behavior of GFP by maintaining linker-centered emission of an HBI-based chromophore while replicating the photoluminescence maxima typical for natural GFP-based systems.[150] In another report, the same group utilized a direct synthesis approach to generate a robust framework containing H_2BDC-BI as a linker to form $Zr_6O_4(OH)_4(BDC\text{-}BI)_6$.[22] This scaffold possessed a significantly different arrangement of chromophores and topology in

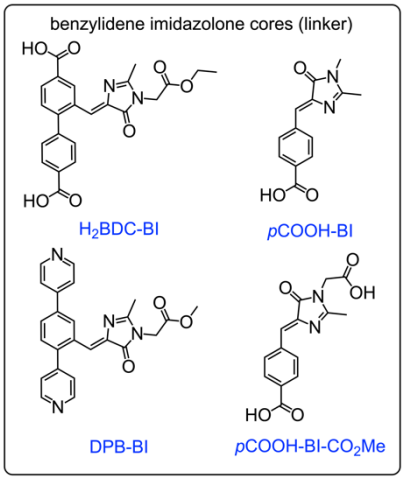

Fig. 18 Structures of BI-based linkers integrated in MOFs.[22,62,66,151]

comparison to the previously formed Zn_4O(BDC-BI). Despite these vast differences in the structure and arrangement of chromophores, similar photoluminescence profiles were observed with emission maxima of 516 nm (λ_{ex} = 365 nm, Zn_4O(BDC-BI)) and 490 nm (λ_{ex} = 360 nm, $Zr_6O_4(OH)_4$(BDC-BI)$_6$).[62,150]

As an alternative approach to control chromophore dynamics, Shustova and coworkers developed a method to anchor only one side of a chromophore to a rigid scaffold (Fig. 17, right), similar to the incorporation of the chromophore in a protein.[22] Two novel chromophores were prepared, *p*COOH-BI (*p*COOH-BI = 4-((1,2-dimethyl-5-oxo-1,5-dihydro-4*H*-imidazol-4-ylidene)methyl)benzoic acid; Fig. 18) and *p*COOH-BI-CO_2Me (4-((1-(carboxymethyl)-2-methyl-5-oxo-1,5-dihydro-4*H*-imidazol-4-ylidene)methyl)benzoic acid; Fig. 18), for integration in NH_2 group-containing frameworks, MIL-101(Al)-NH_2. The resulting emission profiles were shifted to the green region compared to those of the chromophores in the solid state.[22] Anchoring only one side of the chromophore rather than both sides allowed for more freedom for chromophore dynamics while simultaneously preventing leaching from the pores. Overall, this approach could be perceived as a "hybrid" between coordinative immobilization and non-coordinative inclusion.

Non-coordinative immobilization of a BI-donor and a porphyrin-acceptor to achieve better spectral overlap necessary to achieve ET was presented in section 2.1; however, coordinative tethering is another method to promote ET processes. For instance, functionalization of the BI-donor for incorporation into a scaffold was necessary and resulted in preparation of DPB-BI (DPB-BI = methyl-2-(4-(2,5-di(pyridin-4-yl)benzylidene)-2-methyl-5-oxo-4,5-dihydro-1*H*-imidazol-1-yl)acetate; Fig. 18).[66] Immobilization of this chromophore as pillars into layers of Zn_2(ZnTCPP) led to ligand-to-ligand ET efficiency of 65%.[66]

3.2 Photochromic Linkers

Integration of photochromic linkers as a chromophore within the confined space of a MOF matrix allowed for addressing challenges that includes leaching, irreversible photoisomerization (e.g., for spiropyran derivatives), and chromophore alignment and separation that could be crucial for promotion of a photochromic response.[74,82,83] In this section, we will discuss diarylethene- and spiropyran-linkers as two classes that possess distinct routes of photoisomerization (Fig. 3). Diarylethene derivatives are remarkable for their fatigue-resistant photochromic performance, rapid response in the solid state, and thermal stability. Spiropyran moieties pursue a different pathway for photoinduced cyclization reactions compared to diarylethene, while still generating highly-colored photoisomers under UV-irradiation. Diarylethene's photoisomerization is described as a covalent bond formation between the two methylthiophene groups; contrastingly, spiropyran derivatives undergo significant structural changes

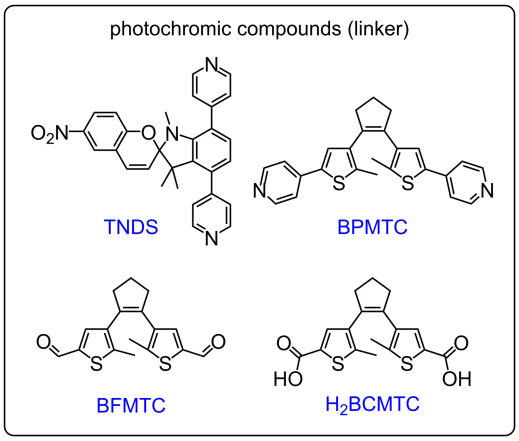

Fig. 19 (*top*) Structures of photoresponsive linkers integrated in MOFs or COFs inside a framework as a side group or a backbone.

centered on the sp^3 "spiro"-carbon rotating from an orthogonal to planar geometry upon photoisomerization.[74] In addition, spiropyran is colorless, hydrophobic, and uncharged, but its isomer, merocyanine, is a colored isomer with a hydrophilic zwitterion. Spiropyran-based compounds typically do not exhibit reversible photoisomerization in the solid state due to the large structural reorganization upon isomerization in contrast to diarylethene derivatives that typically undergo complete reversible photoisomerization in the solid state.[74]

As discussed in section 3.1, the multifaceted nature of the MOF platform opens several pathways of coordinative integration of photoresponsive moieties.[82,151] Depending on geometric constraints and functionalization, photochromic molecules can be integrated into a crystalline scaffold as a part of the framework skeleton, as a side group, and as a capping linker (Fig. 3 and 19). Thus, depending on the nature of the photochromic unit and the choice of framework, the immobilization approach can be selected. For example, a rational way for their integration of spiropyran moieties would be as a side group (compared to backbone), since their photoisomerization promotes large structural transformations and only can occur inside framework cavities. In this section, we will emphasize the unexpected outcomes that can be achieved by merging crystalline porous scaffolds with the dynamic capabilities of photochromic molecules (e.g., solution-like behavior in the solid state, enhanced conductivity values, and controllable ET).

Shustova and coworkers reported integration of a diarylethene derivative, BPMTC (BPMTC = 1,2-bis(2-methyl-5-(pyridin-4-yl)thiophen-3-yl)cyclopent-1-ene; Fig. 19), through coordinative immobilization within a well-defined porphyrin framework, Zn_2(ZnTCPP) (H_4TCPP = tetrakis(4-carboxyphenyl)porphyrin), thus facilitating dynamic control of ET.[84] The estimated ET efficiency of Zn_2(ZnTCPP)(BPMTC) was determined to be modest at 15%, but these results opened an avenue for investigations into "on-demand" ET processes. In

addition to ET investigations, it was noted that the forward and reverse process of photoisomerization occurred at different rates (e.g., 30 min for photoisomerization (λ_{ex} = 365 nm) but 107 min for attenuation (λ_{ex} = 590 nm)).

As a follow-up study, the same group delved further into understanding cycloreversion kinetics of photochromic MOFs.[85] They compared photochromic linkers in the solid state, in solution, and coordinatively immobilized in MOFs (Fig. 20). Two approaches were utilized for integration of the diarylethene derivatives, BPMTC and H_2BCMTC (H_2BCMTC = 4,4′-(cyclopent-1-ene-1,2-diyl)bis(5-methylthiophene-2-carboxylic acid; Fig. 19), into frameworks with different topologies: integration as pillars between layers and as a postsynthetic capping linker, respectively.[85] Zn_2(DBTD)(BPMTC) (H_4DBTD = 3′,6′-dibromo-4′,5′-bis(4-carboxyphenyl)-1[1,1′:2′,1″-tetraphenyl]-4,4″-dicarboxylic acid) was evaluated and revealed a nearly 70 times slower isomerization in comparison to the "free" linker in the solid state. The authors speculate that the marked decrease in rate could be due to the anchoring pyridyl moieties to the metal nodes, restricting photoisomerization that occurs through the linker skeleton. The other approach used by the same team is based on integration of H_2BCMTC as a capping linker into $Zr_6O_4(OH)_8(Me_2BPDC)_4$ (H_2Me_2BPDC = 2,2′-dimethylbiphenyl-4,4′-dicarboxylic acid) coordinated to $Zr_6O_4(OH)_8^{8+}$ nodes.[85] The observed photoisomerization rates of H_2BCMTC in the solid state, in solution, and integrated into the MOF were similar (Fig. 20).[85] The authors hypothesized that H_2BCMTC itself could form a "hydrogen-bonding" framework since the carbonyl and hydroxyl groups on the carboxyl moieties can easily form O–H···O hydrogen bonds.[152] Formation of such a network in the solid state could result in restricted molecular dynamics, similarly to the confined space of a MOF resulting in similar kinetics of photochromic linker. Indeed, the measured rate constants of H_2BCMTC as a capping linker in $Zr_6O_4(OH)_8(Me_2BPDC)_4$ and H_2BCMTC in the solid state were found to be 4.1×10^{-2} s^{-1} and 4.8×10^{-2} s^{-1}, respectively.

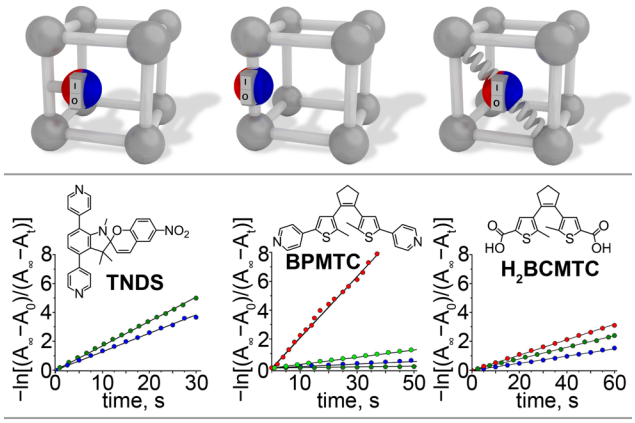

	solid state	solution	MOF
TNDS	*a*	1.2×10^{-1} *b*	1.6×10^{-1}
BPMTC	2.0×10^{-1}	1.0×10^{-2} *b*	2.8×10^{-3}
			2.0×10^{-2}
H_2BCMTC	4.8×10^{-2}	2.6×10^{-2} *c*	4.1×10^{-2}

[a]Photoisomerization was not fully reversible. [b]*C* = 3 mM in DMF. [c]*C* = 3 mM in MeOH.

Fig. 20 (*top*) Photoswitchable molecules coordinatively immobilized as (*left to right*) a side group, a linker, and a capping linker inside the MOF scaffold. (*middle*) Cycloreversion kinetics and (*bottom*) corresponding rate constant of TNDS, BPMTC, and H_2BCMTC as a solid (red), in solution (blue), and immobilized in a MOF (green) upon irradiation with visible light.[85] Reproduced from ref. 85 with permission from American Chemical Society, copyright 2018.

As a next step, Shustova and coworkers turned their attention to a different class of photochromic molecules: spiropyran derivatives. In contrast to diarylethene-based linkers described above, photoisomerization of spiropyran molecules is accompanied with significant structural transformations. Taking the structural aspect into account, the first example of a spiropyran-based MOF, Zn_2(DBTD)(TNDS) (TNDS = 1′,3′,3′-trimethyl-6-nitro-4′,7′-di(pyridin-4-yl)spiro[chromene-2,2′-indoline]; Fig. 19) consists of TNDS linkers integrated between 2D layers.[85] Remarkably, coordinative immobilization of TNDS into the MOF allowed for its photoisomerization that is restricted in the solid state, and moreover, merocyanine-to-spiropyran rates were similar to ones observed for this linker in solution.[85] Thus, the porous nature of the crystalline scaffold can be used for promoting photoisomerization of photochromic linkers that is typically not possible in the solid state due to geometric restrictions.

Combining the possibility of fast isomerization found for spiropyran derivatives integrated inside a framework and the distinct properties of spiropyran and merocyanine photoisomers,[86] the same group subsequently established a correlation between photoisomerization kinetics and MOF electronic properties.[86] To monitor changes in photophysical and electronic properties of materials, conductivity measurements, optical cycling, and spectroscopic analysis were employed. For instance, conductivity measurements performed on bulk powder of Zn_2(DBTD)(TNDS) revealed that conductivity modulation can be achieved even after 15 s of irradiation with UV light. Similarly, they also were able to establish a photophysics–electronic structure correlation for diarylethene-based MOFs.[86] In order to visualize the drastic changes in MOF conductivity as a function of photoswitching in a confined space, the construction of an electric circuit that allowed for LED switching upon exposure to incident light was engineered.[86] Thus, the reported measurements were the first examples displaying a correlation between electronic behavior of crystalline materials and their photophysics.[86]

To expand the principle of electronic property modulation, Zhang and coworkers designed an external-stimulus-active COF by utilizing a diarylethene moiety,[87] BFMTC (BFMTC = 1,2-bis(5-formyl-2-methylthien-3-yl)cyclopentene; Fig 19.), as a COF linker. Their 2D reversible switching thin film exhibited up to a 200-fold enhancement in electrical conductivity after irradiation with UV light. Moreover, they constructed an

electrical circuit to correlate changes in conductivity with irradiation of UV light, in a similar fashion to Shustova and coworkers.[86,87]

3.3 Suppression of Aggregation-Caused Quenching (ACQ) Effect in Frameworks

As described earlier in section 2.6, a MOF can act as a platform for overcoming challenges associated with ACQ (typically exhibited by chromophores in the solid state) by separating chromophores through integration as a linker or by confining a chromophore into the cavity of a MOF or COF (Fig. 21). This section presents proven strategies and progress that has been recently acquired to overcome ACQ by using crystalline scaffolds (MOFs or COFs), portending the potential of extended crystalline structures for solid-state lighting applications.

One strategy to overcome the challenge of ACQ is based on separating the linkers by derivatizing the chromophore core with functional groups for incorporation as a part of the framework backbone. Zhou and coworkers utilized a mixed-ligand approach to synthesize the Zr-based UiO-67 framework[13] with varying ratios of the chromophore, H_2PDCA (H_2PDCA = 3,10-perylene dicarboxylate; Fig. 21), and the nonfluorescent linker, H_2BPDC. Several isoreticular versions of UiO-67 were produced containing both linkers with varying average distances between chromophores resulted in vastly different photophysical properties: photoluminescence maxima, excitation lifetimes, and QYs. The restricted perylene core of $PDCA^{2-}$ in the MOF resulted in a photoluminescence profile with an emission band at 400 nm (λ_{ex} = 300 nm) that matched the emission band of the perylene linker itself. Interestingly, when the MOFs contained >0.35 mol% of the perylene-based linker, an additional emission band at ~520 nm appeared and would increase in intensity as the mol% of $PDCA^{2-}$ increased. This particular band in the emission spectra at ~520 nm was attributed to excimer formation between adjacent perylene linkers. Further increasing the installation of the perylene linker beyond 1.8 mol% led to a decrease in emission intensity of both bands at approximately 400 nm and 520 nm. In addition, fluorescence QYs of several samples were measured. As a result, the highest QY was found for the framework (UiO-67) containing 1.8 mol% of $PDCA^{2-}$.[13] Since perylene derivatives could become emissive when incorporated as a part of the MOF matrix, Zhou and coworkers leveraged this phenomenon by developing a rapid response sensor for O_2. Upon exposure to 5% of O_2, MOF fluorescence was quenched due to ET. Moreover, the performance and structure of the MOFs were maintained for up to five cycles, portending their employment as recyclable fluorescent sensors.

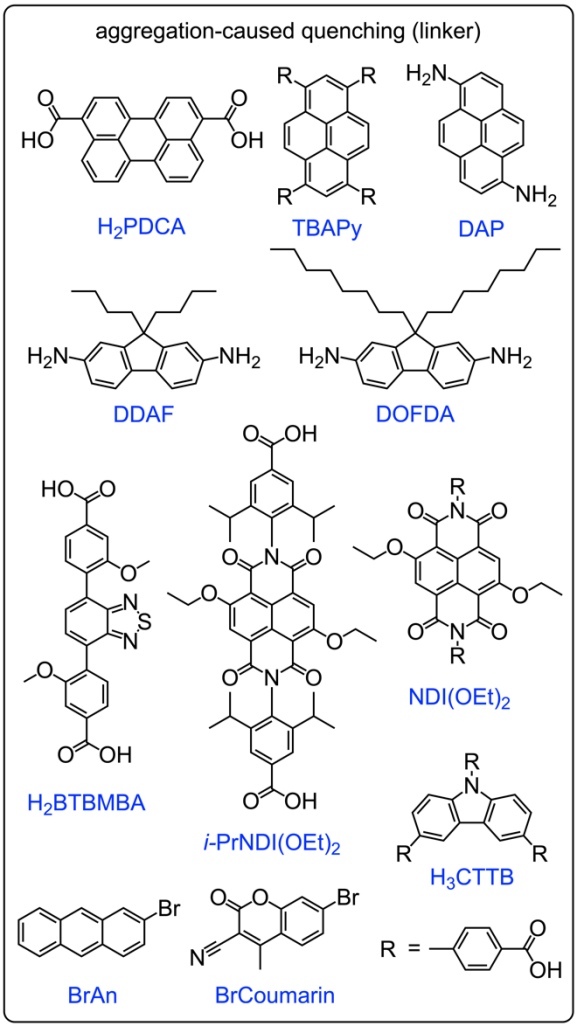

Fig. 21 Structures of linkers exhibiting ACQ effect that were used for integration inside MOFs or COFs.

Skabara and coworkers demonstrated that the ACQ effect observed for benzothiadiazole derivatives could be diminished by confining a benzothiadiazole-based linker, H_2BTBMPBA (H_2BTBPBA = 4,4'-(benzo[*c*][1,2,5]thiadiazole-4,7-diyl)bis(3-methoxybenzoic acid)), inside a UiO-68 analog.[14] A remarkable 116-fold enhancement of the QY was revealed upon comparing the coordinatively immobilized benzothiadiazole-based linker in the MOF matrix with the free linker itself.

Another strategy proven to reduce the ACQ effect of chromophores confined in MOFs or COFs is to control the mutual orientation of chromophores within the host scaffold. In other words, the topological control provided by MOFs and COFs can prevent π–π stacking through spatial and orientational organization of chromophores, and thus, minimize the ACQ effect. For example, Wöll and coworkers prevented ACQ of fluorescence in MOFs by designing a zinc-based surface-anchored MOF (Zn-SURMOF-2) constructed of $NDI(OEt)_2$, ($NDI(OEt)_2$ = 4,4'-(4,9-diethoxy-1,3,6,8-tetraoxo-1,3,6,8-tetrahydrobenzo[*lmn*][3,8]phenanthroline-2,7-diyl)dibenzoic acid; Fig. 21).[153] Integration of NDI-based chromophores inside a MOF allowed for their alignment along the (010) plane. As expected from previous reports on NDI-based MOFs, the close-packing of $NDI(OEt)_2$ (Fig. 21) in Zn-SURMOF-2 led to non-

emissive *H*-aggregates. Remarkably, Wöll and coworkers found that by increasing the rotation angle, ϑ, of the chromophores around the molecular axis (along the carboxyphenyl rings), they were able to suppress *H*-aggregate formation (Fig. 22). By employing theoretical modeling, the authors were able to confirm their hypothesis that increasing the distance between NDI cores and a slipping of the intermolecular transition dipoles would result in a larger rotation angle and reduce fluorescence quenching.[153] The authors calculated the TDM-TDM (transition dipole moment) Coulomb coupling between two R-NDI(OEt)$_2$ chromophores which are 6.8 Å apart as a function of ϑ (where *R* is one of 18 substituents on the NDI core). Calculations based on the transition charge fit discerned that when ϑ > 55.4°, due to bulky substituents on the NDI core, there was a shift in formation of *H*- to *J*-type aggregates (non-emissive to emissive). Moreover, the Zn-SURMOF-2 constructed from *i*-PrNDI(OEt)$_2$ (*i*-PrNDI(OEt)$_2$ = 4,4'-(4,9-diethoxy-1,3,6,8-tetraoxo-1,3,6,8-tetrahydrobenzo[*lmn*][3,8]phenanthroline-2,7-diyl)bis(3,5-diisopropylbenzoic acid); Fig. 21), with isopropyl groups attached to the NDI core, led to a strongly green emissive material (λ_{em} = 540 nm, λ_{ex} = 450 nm) with a QY of 2.3%. Thus, through strategic design and computational planning, the authors demonstrated that they could transform a traditionally non-emissive material to an emissive SURMOF, foreshadowing the possibility for rational formation of *J*-aggregates within a rigid framework.

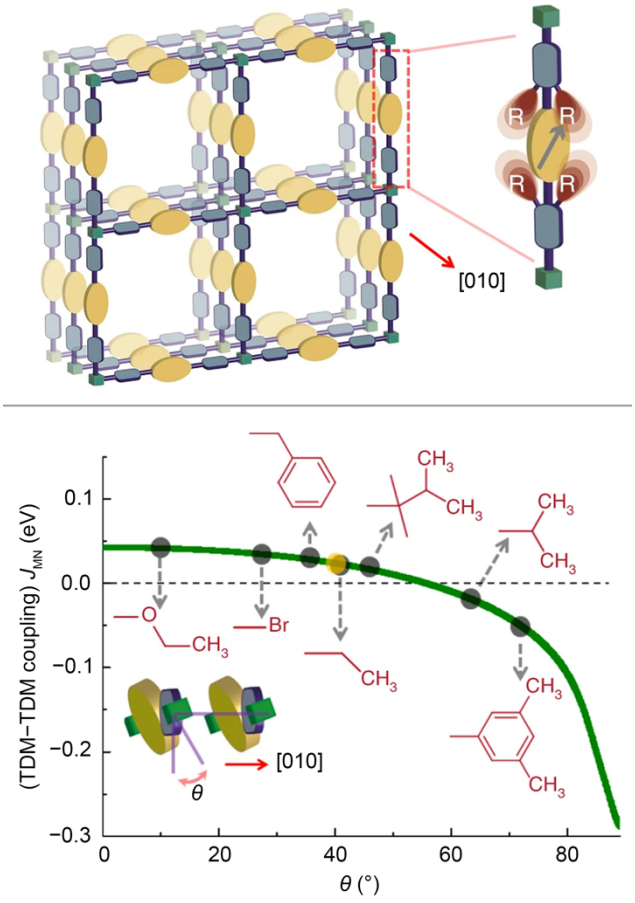

Fig. 22 (*top*) Schematic representation of a Zn-SURMOF-2 structure showing the alignment of chromophores along the [010] plane. Green cube = a Zn-paddle-wheel type secondary building unit, a yellow ellipsoid = NDI(OEt)$_2$, and a gray arrow = transition dipole orientation. (*bottom*) The green line is a plot of calculated Coulomb coupling (transition charge from electrostatic potential method, TrEsp) vs rotation angle, ϑ. The different *R* groups that exert different values of ϑ are illustrated on the graph. The yellow circle on the green line is the predicted ϑ (by GROMACS-2018.4) with *R* = H. Reproduced from ref. 153 with permission from Springer Nature, copyright 2019.

Allendorf and coworkers demonstrated a proof-of-principle study that a MOF could be utilized as a photosensitizer in a PHOTOVOLTAIC device by dispersing nanocrystals of a porphyrin MOF, PPF-4 (PPF = pillared porphyrin framework), on a planar substrate coated with TiO_2 by atomic layer deposition.[154] Similarly, Saha and coworkers strategically grew PPF-11 films with vertically aligned ZnTCPP walls and horizontal 2,2′-dimethyl-4,4′-bipyridine molecules attached to an FTO (fluorine-doped tin oxide) surface.[155] They probed their material as a more effective sensitizer for photovoltaic applications. Under simulated one-sun illumination, their MOF-based dye-sensitized solar cell displayed a PCE of 0.86%.[155]

A different (less-investigated) platform that can be employed to suppress the ACQ effect is a COF. However, these purely organic scaffolds could be challenging to utilize due to potential fluorescence quenching arising from chromophore π-π stacking within the planar two-dimensional (2D) layers. One way to address this issue is the rational design of organic linkers. For example, Wang and coworkers demonstrated that a COF with a semi-planar, contorted structure could behave as a signal transducer by amplifying the fluorescence response.[156] In this study, COF-LZU8 was synthesized from 2,5-bis(3-(ethylthio)propoxy)terephthalohydrazide and BTCA (1,3,5-benzenetricarbaldehyde) linkers. Although both linkers are non-emissive in the solid state, the COF was emissive and had an estimated QY of 3.5%. Interestingly, a fully planar COF constructed from similar building blocks showed negligible fluorescence in the solid state, likely due to ACQ, therefore the contorted structure of the COF could be the key to designing fluorescent organic scaffolds. The strong fluorescent properties of the prepared COF were harnessed as a Hg^{2+} sensor with a remarkable detection limit of 25 parts per billion (ppb).[156]

Another avenue for preventing the ACQ effect is strategic design of a COF with the desirable motif that impacts layer stacking.[157,158] Zamora and coworkers prepared the first example of an imine-linked 2D COF displaying emission in the solid state.[157] The COF, IMDEA-COF-1, constructed from DAP (DAP = 1,6-diaminopyrene; Fig. 21) and BTCA linkers, exhibits green emission, and a photoluminescence QY was found to be 3.5%.[157] Analysis of powder X-ray diffraction (PXRD) patterns confirmed that the COF layers were staggered and caused a decrease in the degree of π–π stacking compared to the eclipsed layer arrangement. In contrast to IMDEA-COF-1, its

counterpart with an eclipsed stacking conformation, IMDEA-COF-2, synthesized from DAP and TP (TP = 2,4,6-triformylphloroglucinol), was not emissive due to interlayer interactions.

Further control over the orientation of layers was investigated by Yin and coworkers.[158] They prevented formation of eclipsed stacking by decorating the chromophores with alkyl chains, and therefore, minimizing interlayer interactions.[158] The authors reported that in this study, alkyl groups decorating the fluorene-based chromophore not only changed the stacking conformation of COFs from eclipsed to staggered but also increased the interlayer distance. Similar to the example described above by Zamora and coworkers, a COF was designed with a linker containing alkyl groups, DDAF (DDAF = 9,9-dibutyl-2,7- diaminofluorene; Fig. 21), to act as a "spacer" and increase the interlayer spacing, promoting a staggered conformation. Through integration of functional groups on the COF linker, the authors demonstrated that a fluorescent COF could be prepared with a fluorescence QY of 10.7%

Spatial chromophore separation can be achieved not only by direct synthesis of a COF (i.e., chromophore = a part of the framework backbone) but also through postsynthetic modification of a COF. For example, Shustova and coworkers demonstrated that integration of coumarin and anthracene (that are nearly non-emissive in the solid state) inside the confined space of a framework, could "turn on" their emission (Fig. 23).[90]

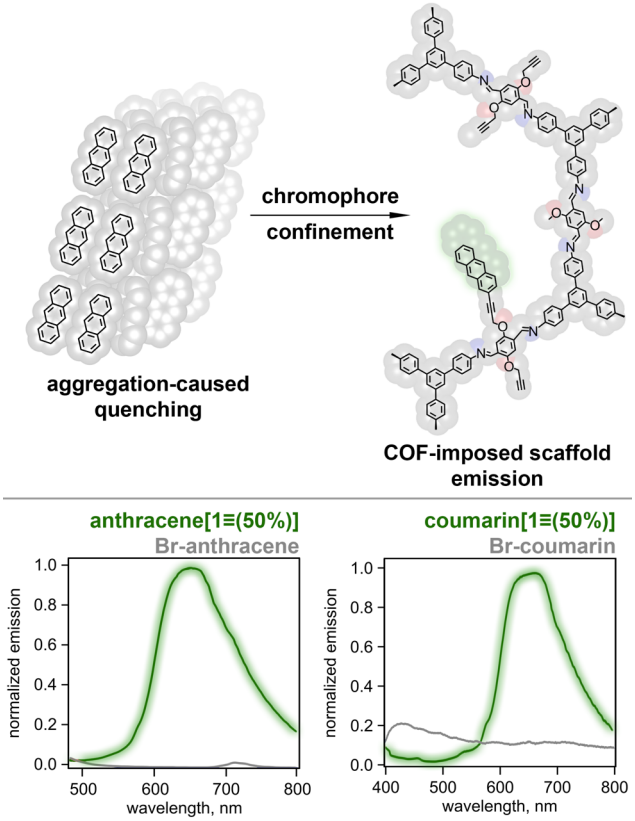

Fig. 23 (*top*) Schematic representation of fluorescent tag integration in a COF. (*left*) Chromophore aggregation in the solid state and (*right*) organization through a COF scaffold. (*bottom left*) Normalized emission spectra of 2-bromoanthracene (gray) and anthracene[1≡(50%)] (green) in the solid state. (*bottom right*) Normalized emission spectra of 6-bromo-3-cyano-4-methylcoumarin (gray) and coumarin[1≡(50%)] (green) in the solid state.[90] Reproduced from ref. 90 with permission from John Wiley and Sons, copyright 2020.

3.4 Spatially Separated Chromophores Exhibiting Aggregation-Induced Emission (AIE)

Rigidification of chromophores via covalent bonds or inter/intra-molecular interactions have been illustrated on several examples (e.g., tetraphenylethylene (TPE), hexaphenylsilole, hexaphenylbenzene, and substituted pyrroles)[145,146,159–163] resulting in emission induction through their molecular aggregation. This phenomenon, referred to as AIE (Fig. 24), is widely applied in biosensing, environmental monitoring, and optoelectronics, e.g., organic light-emitting diodes (OLEDs), phosphor-converted white-light LEDs (PC-wLEDs), liquid crystal displays (LCDs), and luminescent solar concentrators.[164–170] Fluorescence of AIE-based chromophores is generally based on the aggregation of molecules that leads to restriction of intramolecular rotational and vibrational modes (i.e., suppression of non-radiative decay pathways, Fig. 24).[171]

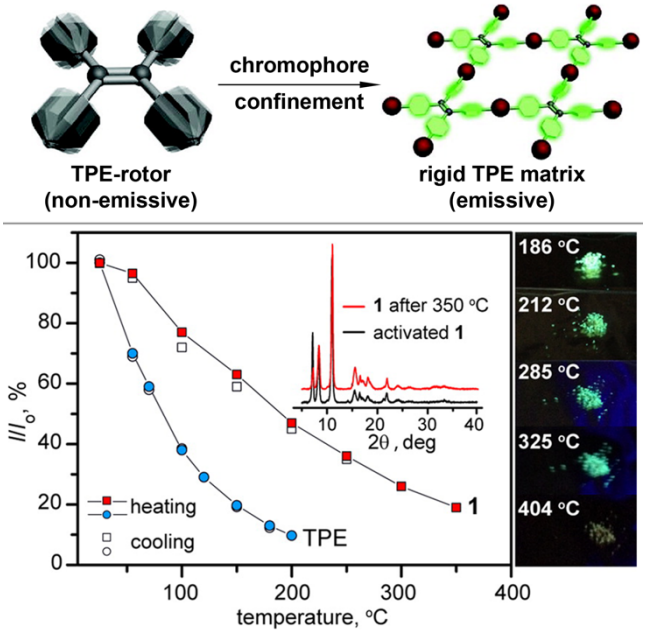

Fig. 24 (*top*) Turn-on luminescence of a non-emissive TPE-core through coordinative immobilization within rigid MOFs. (*bottom*) Normalized temperature-dependent fluorescence decay profiles of a TPE-based MOF (squares) and TPE-linker (circles). The inset shows PXRD patterns of the activated TPE-based MOF and after heating at 350 °C in air. The optical micrographs show the fluorescent TPE-based MOF upon heating at various temperatures in air.[148,149] Reproduced from ref. 148 and ref. 149 with permission from American Chemical Society, copyright 2011 and 2013, respectively.

For instance, this effect can be achieved in the solid state due to molecular packing. However, incorporation of AIE-based chromophores into rigid frameworks such as MOFs and COFs can also result in rigidification of the chromophore backbone through coordinative immobilization, and therefore, the appearance of bright emission.[172] This section of the review will first focus on examples of TPE-based chromophores (as the most widely studied class of AIE chromophores) in MOFs, followed by examples of MOFs containing other AIE-based chromophores such as carborane derivatives,[173] and lastly, examples of COFs containing AIE-chromophores (Fig. 25).

TPE-based derivatives are renowned for bright emission in the solid state, originating from the restriction of phenyl arm rotational and vibrational modes.[174–177] While in dilute solutions, the excited state of TPE will decay non-radiatively, resulting in weak emission.[174,178–180] By restricting the phenyl arms attached to the central ethylene moiety through coordinative immobilization of a TPE fragment in supramolecular ensembles (i.e., as a part of linkers in MOFs and COFs), emission may be restored.[145–147,181] The realization of fluorescent TPE-based MOFs was demonstrated first by Dincă and coworkers in a series of extensive reports.[146,148,149] For instance, by coordinating $TCPE^{4-}$ to Zn^{2+} nodes (H_4TCPE = tetrakis(4-carboxyphenyl)ethylene; Fig. 25), it was shown that geometrical restrictions imposed on the phenyl ring arms impart bright emission that would only be observed in TPE-containing aggregates, despite the chromophores being spatially separated (shortest Ph···Ph distance= 3.28 Å for H_4TCPE and 4.73 Å for $Zn_2(TCPE)$: Fig. 24 and 25).[146,182] Furthermore, it was estimated through quadrupolar spin-echo solid-state ^2H NMR spectroscopy that the activation barrier for the phenyl group rotation within the TPE-based MOF was 43(6) $kJ{\cdot}mol^{-1}$ (20 $kJ{\cdot}mol^{-1}$ higher than that of unrestricted TPE).[146] These findings laid the foundation to apply TPE-based MOFs in engineering selective sensors working at variable temperatures (Fig. 24).[149] Due to the MOF matrix, TPE-centered emission was preserved in air up to 300 °C (Fig. 24). Interestingly, the TPE-based MOF[149] was not selective toward several gaseous analytes (e.g., vapors of triethylamine, ethylenediamine, *N*,*N*-diethylformamide, and water) at room temperature, but at 100 °C, it exhibited high selectivity towards ammonia.[149] Subsequently, TPE-based MOF sensors were reported for the detection of mycotoxins, benzenes, *m*-xylene, mesitylene, nitro explosives, and toxic metal cations.[183]

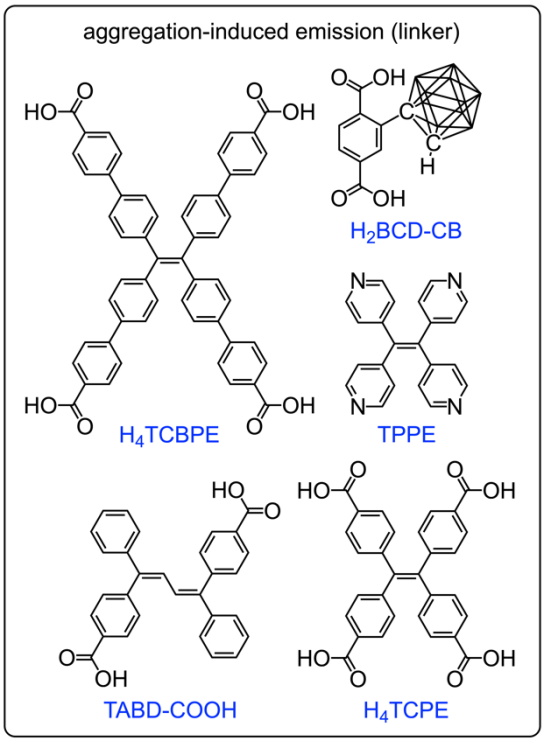

Fig. 25 Structures of AIE-linkers integrated in MOFs or COFs.

In a similar vein, Xu and coworkers published a study on a TPE-derivative, TPPE (TPPE = 1,1,2,2-tetrakis(4-(pyridin-4-yl)phenyl)ethene; Fig. 25), as well as a TPE-based MOF, $[Cd_2(TPPE)(IPA)_2]$ (IPA = isophthalic acid), for its application as a selective solvent sensor and luminescent thermometer.[184] Their studies revealed bright blue emission for TPPE in solution as a function of solvent ratio (e.g., 1000 times increase in intensity in 90:10 v/v H_2O:tetrahydrofuran (THF) compared to pure THF). Immobilization of TPPE within $[Cd_2(TPPE)(IPA)_2]$ revealed solvent-dependent emission attributed to guest-mediated inter-ligand electronic coupling.[185,186] Moreover, they probed $[Cd_2(TPPE)(IPA)_2]$ for its potential as a selective solvent sensor as well as a luminescent thermometer by using electron-rich solvents to fine-tune both $\lambda_{em(max)}$ and photoluminescence intensity.

Guest-mediated photophysical property tuning is only feasible in porous materials, that highlights a fundamental advantage of MOFs in comparison with other reported materials. The porosity of MOFs can be exploited to tailor the material photophysical response through guest-mediated rigidification during guest sorption and desorption processes.[10,146] In this regard, Tang and coworkers reported a silver-chalcogenolate-based MOF, $[Ag_{12}(StBu)_6(CF_3CO_2)_6]_{0.5}[Ag_8(StBu)_4(CF_3CO_2)_4](TPPE)_2$ in which guest molecules allowed for restriction of the intramolecular rotations of TPPE arms.[187] After several sorption-desorption cycles, there was no significant loss of emission intensity, highlighting material recyclability. The detected material behavior was attributed to rigidification of TPE-based chromophores via guest loading promoting AIE.

Separate from sensing, potential applications of TPE-based chromophores in solid-state lighting are contingent on preparation of materials with high QYs and fluorescence tunability for achieving bright intensity at desirable wavelengths. Aggregates of TPE-based chromophores typically have relatively high QYs in the solid state as mentioned before.[188–190] In MOFs that rely on confinement-driven phenyl

ring restriction rather than aggregation, high QYs of TPE-based linkers can still be achieved.[191–194] For instance, Li and coworkers have largely driven the field of MOF-based solid-state lighting with numerous examples of MOFs possessing controllable emission, guest-mediated QYs, and tunable fluorescence lifetimes.[10,18,19,195–197] For instance, a TPE-based MOF, Zn_2(TCBPE) (H_4TCBPE = 4',4'',4''''',4'''''''-(ethene-1,1,2,2-tetrayl)tetrakis ([1,10-biphenyl]-4-carboxylic acid)), possessed a high QY (>95%) due to the TPE-chromophore confinement.[10] The prepared MOF, Zn_2(TCBPE), was shown to have an emission profile and Commission International de l'Eclairage (CIE) coordinates that are almost identical to those of cerium(III)-doped yttrium aluminum garnet (YAG:Ce^{3+}; (0.42, 0.54) for Zn_2(TCBPE) and (0.43, 0.54) for YAG:Ce^{3+}). Therefore, this framework could be considered as an alternative for the replacement of the commonly-used yellow phosphor, YAG:Ce^{3+}, in PC-wLEDs.

The TPE-class of chromophores are undoubtedly the most studied among all AIE-based chromophores integrated in MOFs and COFs.[18,93,175,176,192,193,197] There are, however, other chromophores that display AIE and that can reap the benefits of a confined environment for producing bright fluorescence while being simultaneously spatially separated in a porous matrix. For example, TABD-COOH (TABD-COOH = 4,4'-((*Z*,*Z*)-1,4-diphenylbuta-1,3-diene-1,4-diyl)dibenzoic acid; Fig. 25) prepared by Wang and coworkers[198–200] possessed similar photophysical properties to TPE despite the fact that the ethylene moiety was extended to a diene fragment (Fig. 25). The chromophore itself exhibited a piezo/mechanochromic response in the solid state.[199,200] Three different MOFs were synthesized by heating TABD-COOH (Fig. 25) in the presence of the corresponding metal salts, Mg, Ni, and Co.[198] In this report, the mechanism for fluorescence was attributed to AIE but could be turned off selectively by LMCT due to incomplete *d*-electron valence shells of the metal cations. In particular, the Mg(II)-MOF (d^5) showed bright emission with a high QY of 38.5%; however, due to the LMCT phenomena, QYs of paramagnetic Ni- and Co-MOFs were found to be only 1.12% and 0.15%, respectively.

In another example illustrating AIE-based emission in MOFs, Kim and coworkers synthesized an *ortho*-carborane-containing emissive framework (Fig. 25) in which appearance of emission was attributed to the confinement of carborane clusters within a porous scaffold.[173]

Emission of AIE-based chromophores in MOFs is an ongoing development that undoubtedly will continue to flourish as new discoveries are made. Recently, there's been a shift in design of AIE-based materials towards AIE-based COFs.[147,201] COFs possess many properties similar to MOFs, including crystallinity, porosity, and tunability; however, they provide a different avenue for tunability of framework topology (e.g., formation of periodic columnar π-arrays and inherent π-conjugation). For instance, the Dichtel group reported a detailed study on the emissive properties of a library of two- and three-dimensional (3D) boroxine-linked COFs with the goal of understanding the effect of interlayer arrangement on optical properties.[202] In this report, excitation-emission matrix fluorescence spectroscopic analysis revealed the origin of enhanced QYs in chromophore-containing COFs (in comparison with chromophore solutions). Specifically, they were able to assign the observed optical features to π-exciplex formation that supports hypothesis about through-space electronic communication between 2D COF layers. Therefore, this report specifically highlights the necessity for understanding the effect of interlayer arrangement in extended structures as well as conquers what can sometimes be considered a disadvantage of COFs (the ACQ effect).

Through the use of COFs to connect organic chromophores into highly conjugated π-lattices, the Jiang group was able to promote emission through the combination of pyrene knots and arylyenevinylene linkages.[203] The strategic design of a 2D sp^2 carbon-conjugated COF (sp^2c-COF) with π-conjugation in the entire plane of the COF symbiotically enhanced stability and rigidified the arylyenevinylene linkage. The imparted constraint of radiative decay leads to visible emission through scaffold-based confinement effects. In particular, introduction of the arylyenevinylene linkage and pyrene chromophores into a single COF led to drastic changes in emission maxima compared to that of the pyrene-based linker. For example, free pyrene-based ligand was blue-emissive in H_2O whereas sp^2c-COF dispersed in H_2O was red-emissive. Such a combination of porosity, fluorescence, and presence of selective functional groups (e.g., cyano functionalities on the COF walls) was used by the authors for metal ion sensing through fluorescence quenching. This COF was studied as a fluorescent probe for Cu^{2+} sensing with quenching occurring at concentrations of only 88 ppb of Cu^{2+} in THF with notable selectivity determined in control experiments with both Cu^{2+} and Zn^{2+} cations present.

4. Confinement-Driven Photophysics in Cages

Metal-organic polyhedrons that are also named in literature as coordination cages, metal-organic cages, or porous molecular cages, are paramount as molecular containers for their role in sensing, drug delivery, bioimaging, and as molecular reactors.[204–206] In contrast to MOFs and COFs that are insoluble extended structures, molecular cages offer an opportunity to study host-guest interactions or chromophore molecular conformations through "conventional" methods such as NMR spectroscopy. Due to this advantage, a cage can be used as a replica of a MOF or COF matrix to elucidate dynamics, molecular conformation, or intermolecular interactions of chromophores using SC-XRD (Fig. 26). In many cases, chromophore loading in MOFs is relatively low (a few wt%) and especially taking into account a large pore aperture, can lead to significant crystallographic disorder. Choice of the cage that mimics the pore size and environment allows for minimizing disorder and

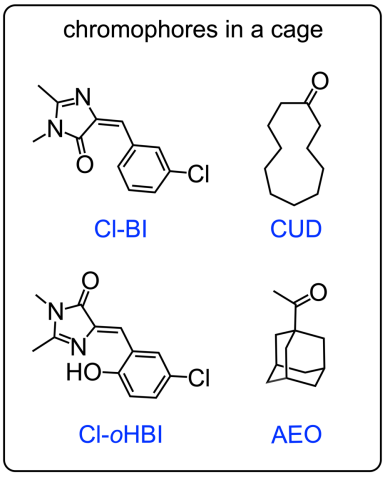

Fig. 26 Structures of chromophores integrated in a $Pd_6(TPT)_4(NO_3)_{12}$ cage and a Zn-TMPA cage.[53,207]

possibly addressing the detected changes in photophysical properties of chromophore@MOF through monitoring chromophore performance inside the cage through spectroscopic analysis and SC-XRD. For instance, Shustova and coworkers detected unusual emission upon encapsulation of Cl-BI (Fig. 26) as a guest inside MOFs which led to a 150 nm bathochromic shift in emission profile of Cl-BI@MOF compared to the chromophore in the solid state.[53] It was hypothesized that such photoluminescent behavior could be correlated with an unusual molecular conformation of the chromophore inside the confined space of a MOF pore. Through the use of a molecular cage, $Pd_6(TPT)_4(NO_3)_{12}$ as a truncated model for a MOF, we were able to discover that a unique chromophore conformation, found in less than 5% of known crystal structures containing HBI-based molecules, was dominant in the confined space of the cage.[53] Transformation of the Cl-BI chromophore conformation in the solid state to inside the confined space of the molecular cage (Fig. 27) requires a *φ*-rotation around the C–C single bond, resulting in the position of the oxygen and chlorine atoms on the imidazolone and phenyl rings, respectively, pointing in opposite directions. Using theoretical modeling, luminescence modulation as a function of different conformations was surveyed demonstrating the fact that a confined environment not only affects Cl-BI chromophore geometry, but also can influence electronic and geometrical structures of the Cl-BI excited states. We also estimated the energy barrier associated with rotation of the single C2–C3 bond by varying the C=C–C=C dihedral angle in the Cl-BI chromophore and found it to be 34.2 kJ/mol.[53] The energy barrier can be further increased to 64.2 kJ/mol in Cl-*o*HBI (Fig. 27) due to intramolecular hydrogen bonding.[53]

Through SC-XRD, the structure of a new conformer formed in the confined environment of $Pd_6(TPT)_4(NO_3)_{12}$ cage was determined (Fig. 27). Based on the support of theoretical calculations, it was speculated that the observed a hypsochromic shift of the photoluminescence maxima for

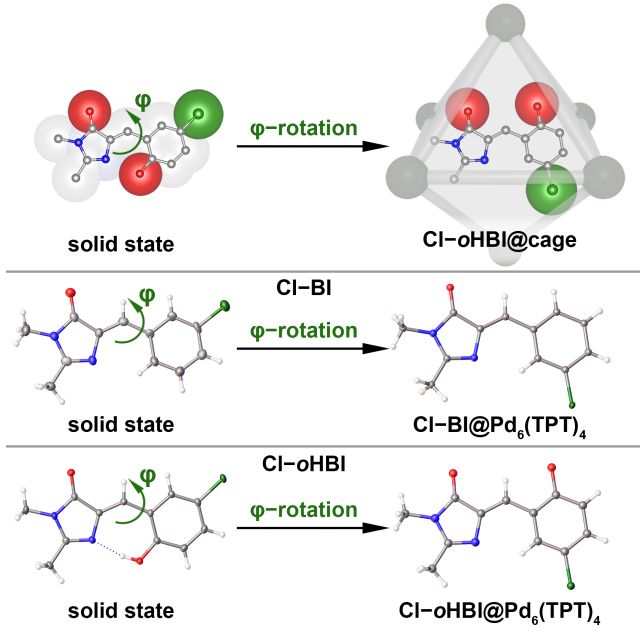

Fig. 27 (*top*) Schematic representation of changes in the molecular conformation of Cl-*o*HBI upon incorporation inside the molecular cage. (*middle* and *bottom*) Crystal structures of Cl-BI and Cl-*o*HBI in the solid state (*left*) and incorporated inside the $Pd_6(TPT)_4(NO_3)_{12}$ cage (*right*). The green, dark blue, gray, red, and white spheres represent chlorine, nitrogen, carbon, oxygen, and hydrogen atoms, respectively. Reproduced from ref. 53 with permission from American Chemical Society, copyright 2020.

Cl-*o*HBI@$Pd_6(TPT)_4(NO_3)_{12}$ compared to the unrestricted chromophore, Cl-*o*HBI is associated with the confined space of the cage and can be potentially explained by disruption of hydrogen bonding.[53] Employing a molecular cage as a truncated model of a MOF allowed for bridging the gap and establishing a correlation between the structure of guest molecules and material photophysical profiles. In addition, the multifunctional capabilities of the molecular cage was illustrated by employing the Cl-*o*HBI@$Pd_6(TPT)_4(NO_3)_{12}$ system as a tool for targeted cargo delivery of Cl-*o*HBI to the confined space of DNA and resulted in promotion of chromophore–DNA interactions.[53]

Conversely, conformation changes of a host can be initiated by the guest.[207] Zonta and coworkers induced a conformation change of a chiral cage, Zn-TMPA (TMPA = *tris*(2-pyridylmethyl)amine), through variation of the guest length.[207] Non-coordinative integration of guests with varying alkyl chain lengths (e.g., succinic acid versus adipic acid) into the cage led to intriguing changes in the circular dichroism profiles.[207] In particular, an increase of the guest length an inversion of the chiroptical absorption in the range of 270–330 nm from negative to positive.[207] Thus, the described diastereodynamic system is the first example in which the guest length can be used to tune the chiral properties of a system, allowing for the development of programmed conformational control.[207]

Ward and coworkers also probed the effect of the guest molecules on cage properties and ET processes.[208] The authors constructed an octanuclear cubic coordination cage with twelve

naphthyl chromophores surrounding the central cavity. Through conventional luminescence titrations, the authors probed the effects of incorporating non-redox active and non-chrompohoric guests and revealed that a flexible guest, CUD (CUD = cycloundecanone; Fig. 26), caused a decrease in photoluminescence intensity; whereas, incorporation of a more rigid guest, AEO (AEO = 1-((3r,5r,7r)-adamantan-1-yl)ethan-1-one; Fig. 26), enhanced the intensity of the photoluminescence response. The authors hypothesized that incorporation of a rigid guest helped to restrict non-radiative decay pathways and incorporation of a flexible guest resulted in the opposite effect. These efforts demonstrate how strategic design of cages and selection of the guest molecule portend a potential avenue to transform traditionally non-emissive moieties into bright photoluminescent materials.

5. Conclusion and Perspectives

As emphasized in this review, MOFs, COFs, and cages have the potential to cause a paradigm shift in the way chromophores are explored. Advancements in tuning chromophore dynamics through confined space-imposed photophysics foreshadows surpassing current technologies, especially as it pertains to porous fluorescence sensors with high spatial resolution.

MOFs, COFs, and cages proffer unrivaled strategic control of chromophore arrangements through the ability to tune distances, angles, and even promote unusual molecular conformations through functionalization of the linkers.[13,22, 53,54, 62,66,145–150,153,157,158] In particular, several reports, primarily from one group, have displayed the ingenuity of engineering artificial scaffolds for mimicking the behavior of GFP and its analogs as an avenue to glean insight into biological processes or preparation of materials with directional ET; however, there are many proteins that have yet to be investigated and fundamental correlations have to be built to fully harness the potential of frameworks as a rigid multifunctional host.

Both AIE and ACQ phenomena can be also addressed through utilization of rigid porous scaffold for development of efficient solid-state lighting materials. The area of AIE-based crystalline scaffolds has benefited largely from the embedment of TPE-based chromophores but a shift in the rather unexplored direction of other AIE-based chromophores could significantly advance this area of MOF-based photoluminescent materials.

An overview of the photophysical data of RuBpy and OsBpy encapsulated MOFs presented in section 2.3 revealed the effects of confinement on the transition metal complexes within very restrictive cavities only achievable through a templated approach (i.e., dimensions similar to that of the encapsulated guest). These results are revealed as an extension of the emission lifetime and shifts in the steady-state emission spectra that are highly dependent upon the nature of the cavity. One of the most significant impacts of confinement in this case is the effect on the energy barrier to access the excited states beyond the lowest energy ^{3}MLCT state (either the excited ^{3}LF or other higher energy ^{3}MLCT states). For instance, tightly restricted cavities increase the barrier between the lowest energy ^{3}MLCT and other higher energy states, regardless of the type of cavity while the energy level of the lowest energy ^{3}MLCT is dependent upon the size and polarity of the cavity. Cavities that allow for solvent access tend to have lower energy ^{3}MLCT states while those that are more restrictive to solvent access tend to increase the ^{3}MLCT state energy. These observations are important for the future design of photoactive MOFs for photocatalytic and light-harvesting applications with tunable photophysical properties.

To summarize, MOFs, COFs, and cages have demonstrated unparalleled potential for confining chromophores and inducing unprecedented photophysical properties. The established field of MOFs has led this area of investigation, but COFs and cages have displayed that they can be employed as a robust, crystalline platform as well. The less-investigated field of COFs has proven to alleviate some concerns relevant to non-radiative decay (e.g., using boroxine instead of imine linkages), and we anticipate that investigation of COFs as a multivariate tool will commence in earnest over the next decade. While photophysics of chromophores has been probed appreciably over the years, discovering intriguing responses of a scaffold-imposed confined space on chromophores is only the tip of the iceberg.

Conflicts of interest

There are no conflicts to declare.

Acknowledgements

This work was supported by the NSF CAREER Award (DMR-1553634). N.B.S thanks the Cottrell Scholar Award from the Research Corporation for Science Advancement, Sloan Research Fellowship provided by Alfred P. Sloan Foundation, Camille Dreyfus Teaching-Scholar Award provided by Henry and Camille Dreyfus Foundation, and the IAS Hans Fischer Fellowship.

Notes and references

1 B. Pattengale and J. Huang, *Phys. Chem. Chem. Phys.*, 2018, **20**, 14884–14888.
2 X.-Y. Liu, Y. Li, C.-K. Tsung and J. Li, *Chem. Commun.*, 2019, **55**, 10669–10672.
3 Z. Wang, B. Wang, Y. Yang, Y. Cui, Z. Wang, B. Chen and G. Qian, *ACS Appl. Mater. Interfaces*, 2015, **7**, 20999–21004.
4 Y. Jiang, J. Park, P. Tan, L. Feng, X.-Q. Liu, L.-B. Sun and H.-C. Zhou, *J. Am. Chem. Soc.*, 2020, **141**, 8221–8227.

5 T. A. Goetjen, J. Liu, Y. Wu, J. Sui, X. Zhang, J. T. Hupp and O. K. Farha, *Chem. Commun.*, 2020, **56**, 10409–10418.
6 A. Khatun, D. K. Panda, N. Sayresmith, M. G. Walter and S. Saha, *Inorg. Chem.*, 2019, **58**, 12707–12715.
7 A. Torres-Huerta, D. Galicia-Badillo, A. Aguilar-Granda, J. T. Bryant, F. J. Uribe-Romo and B. Rodríguez-Molina, *Chem. Sci.*, 2020, **11**, 11579–11583.
8 D. A. Vazquez-Molina, G. M. Pope, A. A. Ezazi, J. L. Mendoza-Cortes, J. K. Harper and F. J. Uribe-Romo, *Chem. Commun.*, 2018, **54**, 6947–6950.
9 S. Jensen, K. Tan, W. P. Lustig, D. S. Kilin, J. Li, Y. J. Chabal and T. Thonhauser, *Chem. Mater.*, 2019, **31**, 7933–7940.
10 W. P. Lustig, S. J. Teat and J. Li, *J. Mater. Chem. C*, 2019, **7**, 14739–14744.
11 N. C. Flanders, M. S. Kirschner, P. Kim, T. J. Fauvell, A. M. Evans, W. Helweh, A. P. Spencer, R. D. Schaller, W. R. Dichtel and L. X. Chen, *J. Am. Chem. Soc.*, 2020, **142**, 14957–14965.
12 N. A. Sayresmith, A. Saminathan, J. K. Sailer, S. M. Patberg, K. Sandor, Y. Krishnan and M. G. Walter, *J. Am. Chem. Soc.*, 2019, **141**, 18780–18790.
13 J. Li, S. Yuan, J. S. Qin, L. Huang, R. Bose, J. Pang, P. Zhang, Z. Xiao, K. Tan, A. V. Malko, T. Cagin and H.-C. Zhou, *ACS Appl. Mater. Interfaces*, 2020, **12**, 26727–26732.
14 E. Angioni, R. J. Marshall, N. J. Findlay, J. Bruckbauer, B. Breig, D. J. Wallis, R. W. Martin, R. S. Forgan and P. J. Skabara, *J. Mater. Chem. C*, 2019, **7**, 2394–2400.
15 J. M. Rowe, E. M. Soderstrom, J. Zhu, P. M. Usov and A. J. Morris, *Can. J. Chem.*, 2018, **96**, 875–880.
16 W. J. Newsome, S. Ayad, J. Cordova, E. W. Reinheimer, A. D. Campiglia, J. K. Harper, K. Hanson and F. J. Uribe-Romo, *J. Am. Chem. Soc.*, 2019, **141**, 11298–11303.
17 W. J. Newsome, A. Chakraborty, R. T. Ly, G. S. Pour, D. C. Fairchild, A. J. Morris and F. J. Uribe-Romo, *Chem. Sci.*, 2020, **11**, 4391–4396.
18 X.-Y. Liu, W. P. Lustig and J. Li, *ACS Energy Lett.*, 2020, **5**, 2671–2680.
19 Y. Lin, L. Yu, H. Wang and J. Li, *CrystEngComm*, 2020, **22**, 5946–5948.
20 Y.-P. Xia, C.-X. Wang, L.-C. An, D.-S. Zhang, T.-L. Hu, J. Xu, Z. Chang and X.-H. Bu, *Inorg. Chem. Front.*, 2018, **5**, 2868–2874.
21 X. Li, J. Yu, D. J. Gosztola, H. C. Fry and P. Deria, *J. Am. Chem. Soc.*, 2019, **141**, 16849–16857.
22 E. A. Dolgopolova, T. M. Moore, O. A. Ejegbavwo, P. J. Pellechia, M. D. Smith and N. B. Shustova, *Chem. Commun.*, 2017, **53**, 7361–7364.
23 A. Van Wyk, T. Smith, J. Park and P. Deria, *J. Am. Chem. Soc.*, 2018, **140**, 2756–2760.
24 J. Lu, B. Pattengale, Q. Liu, S. Yang, S. Li, J. Huang and J. Zhang, *J. Am. Chem. Soc.*, 2018, **140**, 13719–13725.
25 H. Weiss, H.-W. Cheng, J. Mars, H. Li, C. Merola, F. U. Renner, V. Honkimäki, M. Valtiner and M. Mezger, *Langmuir*, 2019, **35**, 16679–16692.
26 J. S. Rao and L. Cruz, *J. Phys. Chem. B*, 2013, **117**, 3707–3719.
27 O. V. Stepanenko, O. V. Stepanenko, I. M. Kuznetsova, V. V. Verkhusha and K. K. Turoverov, in *International Review of Cell and Molecular Biology*, ed. K. W. Jeon, Academic Press, 2013, vol. 302, pp. 221–278.
28 L. Zhu and Y.-B. Zhang, *Molecules*, 2017, **22**, 1149.
29 J. Ozdemir, I. Mosleh, M. Abolhassani, L. F. Greenlee, R. R. Beitle and M. H. Beyzavi, *Front. Energy Res.*, 2019, **7**, 77.
30 M. B. Majewski, A. J. Howarth, P. Li, M. R. Wasielewski, J. T. Hupp and O. K. Farha, *CrystEngComm*, 2017, **19**, 4082–4091.
31 R. J. Drout, L. Robison and O. K. Farha, *Coord. Chem. Rev.*, 2019, **381**, 151–160.
32 T.-H. Wei, S.-H. Wu, Y.-D. Huang, W.-S. Lo, B. P. Williams, S.-Y. Chen, H.-C. Yang, Y.-S. Hsu, Z.-Y. Lin, X.-H. Chen, P.-E. Kuo, L.-Y. Chou, C.-K. Tsung, and F.-K. Shieh, *Nat. Commun.*, 2019, **10**, 5002.
33 J.-S. Qin, S. Yuan, C. Lollar, J. Pang, A. Alsalme and H.-C. Zhou, *Chem. Commun.*, 2018, **54**, 4231–4249.
34 S.-Y. Chen, W.-S. Lo, Y.-Da Huang, X. Si, F.-S. Liao, S.-W. Lin, B. P. Williams, T.-Q. Sun, H.-W. Lin, Y. An, T. Sun, Y. Ma, H.-C. Yang, L.-Y. Chou, F.-K. Shieh and C.-K. Tsung, *Nano Lett.*, 2020, **20**, 6630–6635.
35 Y. Ye, R.-B. Lin, H. Cui, A. Alsalme, W. Zhou, T. Yildirim, Z. Zhang, S. Xiang and B. Chen, *Dalton Trans.*, 2020, **49**, 3658–3661.
36 X. Zhang, L. Li, J.-X. Wang, H.-M. Wen, R. Krishna, H. Wu, W. Zhou, Z. N. Chen, B. Li, G. Qian and B. Chen, *J. Am. Chem. Soc.*, 2020, **142**, 633–640.
37 R.-B. Lin, S. Xiang, H. Xing, W. Zhou and B. Chen, *Coord. Chem. Rev.*, 2019, **378**, 87–103.
38 F. Yu, B.-Q. Hu, X.-N. Wang, Y.-M. Zhao, J.-L. Li, B. Li and H.-C. Zhou, *J. Mater. Chem. A*, 2020, **8**, 2083–2089.
40 S. Das, J. Feng and W. Wang, *Annu. Rev. Chem. Biomol. Eng.*, 2020, **11**, 131–153.
41 J. Li, X. Zhou, J. Wang and X. Li, *Ind. Eng. Chem. Res.*, 2019, **58**, 15394–15406.
42 S. Yuan, X. Li, J. Zhu, G. Zhang, P. Van Puyvelde and B. Van Der Bruggen, *Chem. Soc. Rev.*, 2019, **48**, 2665–2681.
43 R.-B. Lin, S. Xiang, W. Zhou and B. Chen, *Chem*, 2020, **6**, 337–363.
44 J. A. Mason, M. Veenstra and J. R. Long, *Chem. Sci.*, 2014, **5**, 32–51.
45 Y. He, F. Chen, B. Li, G. Qian, W. Zhou and B. Chen, *Coord. Chem. Rev.*, 2018, **373**, 167–198.
46 H. Li, K. Wang, Y. Sun, C. T. Lollar, J. Li and H.-C. Zhou, *Mater. Today*, 2018, **21**, 108–121.
47 M. Li, S. Qiao, Y. Zheng, Y. H. Andaloussi, X. Li, Z. Zhang, A. Li, P. Cheng, S. Ma and Y. Chen, *J. Am. Chem. Soc.*, 2020, **142**, 6675–6681.
48 K. Geng, T. He, R. Liu, S. Dalapati, K. T. Tan, Z. Li, S. Tao, Y. Gong, Q. Jiang and D. Jiang, *Chem. Rev.*, 2020, **120**, 8814–8933.
49 M. Zhang, M. Bosch, T. Gentle and H.-C. Zhou, *CrystEngComm*, 2014, **16**, 4069–4083.
50 A. Schoedel, M. Li, D. Li, M. O'Keeffe and O. M. Yaghi, *Chem. Rev.*, 2016, **116**, 12466–12535.
51 F. Beuerle and B. Gole, *Angew. Chem. Int. Ed.*, 2018, **57**, 4850–4878.
52 Y. Inokuma, T. Arai and M. Fujita, *Nat. Chem.*, 2010, **2**, 780–783.
53 E. A. Dolgopolova, A. A. Berseneva, M. S. Faillace, O. A. Ejegbavwo, G. A. Leith, S. W. Choi, H. N. Gregory, A. M. Rice, M. D. Smith, M. Chruszcz, S. Garashchuk, K. Mythreye and N. B. Shustova, *J. Am. Chem. Soc.*, 2020, **142**, 4769–4783.
54 T. Zhao, J. Han, X. Jin, M. Zhou, Y. Liu, P. Duan and M. Liu, *Research*, 2020, **2020**, 6452123.
55 A. Bajpai, A. Mukhopadhyay, M. S. Krishna, S. Govardhan and J. N. Moorthy, *Int. Union Crystallogr.*, 2015, **2**, 552–562.
56 W.-G. Choi, S. J. Swanson and S. Gilroy, *Plant J.*, 2012, **70**, 118–128.
57 T. M. Roberts, F. Rudolf, A. Meyer, R. Pellaux, E. Whitehead, S. Panke and M. Held, *Sci. Rep.*, 2016, **6**, 28166.
58 M. Zimmer, *Chem. Soc. Rev.*, 2009, **38**, 2823–2832.
59 H. Niwa, S. Inouye, T. Hirano, T. Matsuno, S. Kojima, M. Kubota, M. Ohashi and F. I. Tsuji, *Proc. Natl. Acad. Sci. U. S. A.*, 1996, **93**, 13617–13622.

60 L. M. Tolbert, A. Baldridge, J. Kowalik and K. M. Solntsev, *Acc. Chem. Res.*, 2012, **45**, 171–181.
61 S. R. Meech, *Chem. Soc. Rev.*, 2009, **38**, 2922–2934.
62 E. A. Dolgopolova, T. M. Moore, W. B. Fellows, M. D. Smith and N. B. Shustova, *Dalton Trans.*, 2016, **45**, 9884–9891.
63 M. Yamashina, M. M. Sartin, Y. Sei, M. Akita, S. Takeuchi, T. Tahara and M. Yoshizawa, *J. Am. Chem. Soc.*, 2015, **137**, 9266–9269.
64 F. Jia, H. V. Schröder, L. P. Yang, C. Von Essen, S. Sobottka, B. Sarkar, K. Rissanen, W. Jiang and C. A. Schalley, *J. Am. Chem. Soc.*, 2020, **142**, 3306–3310.
65 E. A. Dolgopolova, A. M. Rice, M. D. Smith and N. B. Shustova, *Inorg. Chem.*, 2016, **55**, 7257–7264.
66 E. A. Dolgopolova, D. E. Williams, A. B. Greytak, A. M. Rice, M. D. Smith, J. A. Krause and N. B. Shustova, *Angew. Chem. Int. Ed.*, 2015, **54**, 13639–13643.
67 D. E. Williams, E. A. Dolgopolova, D. C. Godfrey, E. D. Ermolaeva, P. J. Pellechia, A. B. Greytak, M. D. Smith, S. M. Avdoshenko, A. A. Popov and N. B. Shustova, *Angew. Chem. Int. Ed.*, 2016, **55**, 9070–9074.
68 G. A. Leith, A. A. Berseneva, A. Mathur, K. C. Park and N. B. Shustova, *Trends Chem.*, 2020, **2**, 367–382.
69 M. C. So, G. P. Wiederrecht, J. E. Mondloch, J. T. Hupp and O. K. Farha, *Chem. Commun.*, 2015, **51**, 3501–3510.
70 T. Zhang and W. Lin, *Chem. Soc. Rev.*, 2014, **43**, 5982–5993.
71 L. Yu, K. Fan, T. Duan, X. Chen, R. Li and T. Peng, *ACS Sustain. Chem. Eng.*, 2014, **2**, 718–725.
72 W. Wu, S. Ji, W. Wu, J. Shao, H. Guo, T. D. James and J. Zhao, *Chem. Eur. J.*, 2012, **18**, 4953–4964.
73 W. A. Maza, A. J. Haring, S. R. Ahrenholtz, C. C. Epley, S. Y. Lin and A. J. Morris, *Chem. Sci.*, 2016, **7**, 719–727.
74 A. M. Rice, C. R. Martin, V. A. Galitskiy, A. A. Berseneva, G. A. Leith and N. B. Shustova, *Chem. Rev.*, 2020, **120**, 8790–8813.
75 P. Li, Q. Sui, M. Y. Guo, S. L. Yang, R. Bu and E. Q. Gao, *Chem. Commun.*, 2020, **56**, 5929–5932.
76 H. Zhang, T. Sheng, S. Hu, C. Zhuo, R. Fu, Y. Wen, H. Li and X. Wu, *J. Mater. Chem. C*, 2016, **4**, 3431–3436.
77 H. He, E. Ma, Y. Cui, J. Yu, Y. Yang, T. Song, C. De Wu, X. Chen, B. Chen and G. Qian, *Nat. Commun.*, 2016, **7**, 11087.
78 E. A. Dolgopolova, A. M. Rice, C. R. Martin and N. B. Shustova, *Chem. Soc. Rev.*, 2018, **47**, 4710–4728.
79 H. M. D. Bandara and S. C. Burdette, *Chem. Soc. Rev.*, 2012, **41**, 1809–1825.
80 J. He, K. Aggarwal, N. Katyal, S. He, E. Chiang, S. G. Dunning, J. E. Reynolds, A. Steiner, G. Henkelman, E. L. Que and S. M. Humphrey, *J. Am. Chem. Soc.*, 2020, **142**, 6467–6471.
81 D. Hermann, H. A. Schwartz, M. Werker, D. Schaniel and U. Ruschewitz, *Chem. Eur. J.*, 2019, **25**, 3606–3616.
82 F. Bigdeli, C. T. Lollar, A. Morsali and H.-C. Zhou, *Angew. Chem. Int. Ed.*, 2020, **59**, 4652–4669.
83 D. Hermann, H. Emerich, R. Lepski, D. Schaniel and U. Ruschewitz, *Inorg. Chem.*, 2013, **52**, 2744–2749.
84 D. E. Williams, J. A. Rietman, J. M. Maier, R. Tan, A. B. Greytak, M. D. Smith, J. A. Krause and N. B. Shustova, *J. Am. Chem. Soc.*, 2014, **136**, 11886–11889.
85 D. E. Williams, C. R. Martin, E. A. Dolgopolova, A. Swifton, D. C. Godfrey, O. A. Ejegbavwo, P. J. Pellechia, M. D. Smith and N. B. Shustova, *J. Am. Chem. Soc.*, 2018, **140**, 7611–7622.
86 E. A. Dolgopolova, V. A. Galitskiy, C. R. Martin, H. N. Gregory, B. J. Yarbrough, A. M. Rice, A. A. Berseneva, O. A. Ejegbavwo, K. S. Stephenson, P. Kittikhunnatham, S. G. Karakalos, M. D. Smith, A. B. Greytak, S. Garashchuk and N. B. Shustova, *J. Am. Chem. Soc.*, 2019, **141**, 5350–5358.
87 F. Yu, W. Liu, B. Li, D. Tian, J. Zuo and Q. Zhang, *Angew. Chem. Int. Ed.*, 2019, **58**, 16101–16104.
88 H. A. Schwartz, S. Olthof, D. Schaniel, K. Meerholz and U. Ruschewitz, *Inorg. Chem.*, 2017, **56**, 13100–13110.
89 I. M. Walton, J. M. Cox, J. A. Coppin, C. M. Linderman, D. G. Patel and J. B. Benedict, *Chem. Commun.*, 2013, **49**, 8012–8014.
90 G. A. Leith, A. M. Rice, B. J. Yarbrough, A. A. Berseneva, R. T. Ly, C. N. Buck, D. Chusov, A. J. Brandt, D. A. Chen, B. W. Lamm, M. Stefik, K. S. Stephenson, M. D. Smith, A. K. Vannucci, P. J. Pellechia, S. Garashchuk and N. B. Shustova, *Angew. Chem. Int. Ed.*, 2020, **59**, 6000–6006.
91 A. Dolbecq, P. Mialane, B. Keita and L. Nadjo, *J. Mater. Chem.*, 2012, **22**, 24509–24521.
92 J. Otsuki, *J. Mater. Chem. A*, 2018, **6**, 6710–6753.
93 R. S. Lumpkin, E. M. Kober, L. A. Worl, Z. Murtaza and T. J. Meyer, *J. Phys. Chem.*, 1990, **94**, 239–243.
94 E. M. Kober, B. P. Sullivan, W. J. Dressick, J. V. Caspar and T. J. Meyer, *J. Am. Chem. Soc.*, 1980, **102**, 7383–7385.
95 D. E. Lacky, B. J. Pankuch and G. A. Crosby, *J. Phys. Chem.*, 1980, **84**, 2068–2074.
96 J. M. Mayers and R. W. Larsen, *Polyhedron*, 2019, **171**, 382–388.
97 D. Pomeranc, V. Heitz, J. C. Chambron and J. P. Sauvage, *J. Am. Chem. Soc.*, 2001, **123**, 12215–12221.
98 J. M. Mayers and R. W. Larsen, *Inorg. Chem.*, 2020, **59**, 7761–7767.
99 A. Gualandi, M. Marchini, L. Mengozzi, M. Natali, M. Lucarini, P. Ceroni and P. G. Cozzi, *ACS Catal.*, 2015, **5**, 5927–5931.
100 P. A. Anderson, G. F. Strouse, J. A. Treadway, F. R. Keene and T. J. Meyer, *Inorg. Chem.*, 1994, **33**, 3863–3864.
101 R. W. Larsen and L. Wojtas, *J. Solid State Chem.*, 2017, **247**, 77–82.
102 N. L. Rosi, J. Eckert, M. Eddaoudi, D. T. Vodak, J. Kim, M. O'Keeffe and O. M. Yaghi, *Science.*, 2003, **300**, 1127–1129.
103 O. K. Farha, I. Eryazici, N. C. Jeong, B. G. Hauser, C. E. Wilmer, A. A. Sarjeant, R. Q. Snurr, S. T. Nguyen, A. Ö. Yazaydin and J. T. Hupp, *J. Am. Chem. Soc.*, 2012, **134**, 15016–15021.
104 R. Grünker, V. Bon, P. Müller, U. Stoeck, S. Krause, U. Mueller, I. Senkovska and S. Kaskel, *Chem. Commun.*, 2014, **50**, 3450–3452.
105 S. Ullah, M. A. Bustam, M. A. Assiri, A. G. Al-Sehemi, M. Sagir, F. A. Abdul Kareem, A. E. I. Elkhalifah, A. Mukhtar and G. Gonfa, *Microporous Mesoporous Mater.*, 2019, **288**, 109569.
106 C. R. McKeithan, J. M. Mayers, L. Wojtas and R. W. Larsen, *Inorganica Chim. Acta*, 2018, **483**, 1–5.
107 J. Lu, A. Mondal, B. Moulton and M. J. Zaworotko, *Angew. Chem. Int. Ed.*, 2001, **40**, 2113–2116.
108 R. W. Larsen and L. Wojtas, *J. Phys. Chem. A*, 2012, **116**, 7830–7835.
109 R. W. Larsen, J. M. Mayers, A. A. Alanazi, C. R. McKeithan and L. Wojtas, in *Structure and Bonding*, Springer, Berlin, Heidelberg, 2020, pp. 1–30.
110 S. J. Hug and S. G. Boxer, *Inorganica Chim. Acta*, 1996, **242**, 323–327.
111 C. L. Whittington, L. Wojtas and R. W. Larsen, *Inorg. Chem.*, 2014, **53**, 160–166.
112 C. L. Whittington, L. Wojtas, W. Y. Gao, S. Ma and R. W. Larsen, *Dalton Trans.*, 2015, **44**, 5331–5337.
113 C. R. McKeithan, L. Wojtas and R. W. Larsen, *Inorganica Chim. Acta*, 2019, **496**, 119034.
114 R. W. Larsen, J. M. Mayers and L. Wojtas, *Datlon Trans.*, 2017, **46**, 12711–12716.

115 D. Bradshaw, S. El-Hankari and L. Lupica-Spagnolo, *Chem. Soc. Rev.*, 2014, **43**, 5431–5443.
116 M. L. Hu, M. Y. Masoomi and A. Morsali, *Coord. Chem. Rev.*, 2019, **387**, 415–435.
117 H. Kim and M. S. Lah, *Dalton Trans.*, 2017, **46**, 6146–6158.
118 N. Zhao, K. Cai and H. He, *Dalton Trans.*, 2020, **49**, 11467–11479.
119 J. Kim, B. Chen, T. M. Reineke, H. Li, M. Eddaoudi, D. B. Moler, M. O'Keeffe and O. M. Yaghi, *J. Am. Chem. Soc.*, 2001, **123**, 8239–8247.
120 P. Lainé, M. Lanz and G. Calzaferri, *Inorg. Chem.*, 1996, **35**, 3514–3518.
121 H. Li, M. Eddaoudi, M. O'Keeffe, O. M. Yaghi, *Nature*, 1999, **402**, 276–279.
122 Y. Bai, Y. Dou, L. H. Xie, W. Rutledge, J. R. Li and H.-C. Zhou, *Chem. Soc. Rev.*, 2016, **45**, 2327–2367.
123 Z. Chen, S. L. Hanna, L. R. Redfern, D. Alezi, T. Islamoglu and O. K. Farha, *Coord. Chem. Rev.*, 2019, **386**, 32–49.
124 J. Ru, X. Wang, F. Wang, X. Cui, X. Du and X. Lu, *Ecotoxicol. Environ. Saf.*, 2021, **208**, 111577.
125 J. Winarta, B. Shan, S. M. McIntyre, L. Ye, C. Wang, J. Liu and B. Mu, *Cryst. Growth Des.*, 2020, **20**, 1347–1362.
126 F. Bella, R. Bongiovanni, R. S. Kumar, M. A. Kulandainathan and A. M. Stephan, *J. Mater. Chem. A*, 2013, **1**, 9033–9036.
127 K. Nozaki, K. Takamori, Y. Nakatsugawa and T. Ohno, *Inorg. Chem.*, 2006, **45**, 6161–6178.
128 J. F. Endicott and Y. J. Chen, *Coord. Chem. Rev.*, 2007, **251**, 328–350.
129 K. M. Dean and A. E. Palmer, *Nat. Chem. Biol.*, 2014, **10**, 512–523.
130 G. Crivat and J. W. Taraska, *Trends Biotechnol.*, 2012, **30**, 8–16.
131 C. P. Toseland, *J. Chem. Biol.*, 2013, **6**, 85–95.
132 X.-Y. Liu, K. Xing, Y. Li, C.-K. Tsung and J. Li, *J. Am. Chem. Soc.*, 2019, **141**, 14807–14813.
133 D. Tian, X.-J. Liu, R. Feng, J.-L. Xu, J. Xu, R.-Y. Chen, L. Huang and X.-H. Bu, *ACS Appl. Mater. Interfaces*, 2018, **10**, 5618–5625.
134 Y. Cui, T. Song, J. Yu, Y. Yang, Z. Wang and G. Qian, *Adv. Funct. Mater.*, 2015, **25**, 4796–4802.
135 Y. Tang, W. Cao, L. Yao, Y. Cui, Y. Yu and G. Qian, *J. Mater. Chem. C*, 2020, **8**, 12308–12313.
136 B. Ruan, J. Yang, Y. J. Zhang, N. Ma, D. Shi, T. Jiang and F. C. Tsai, *Talanta*, 2020, **218**, 121207.
137 H. Li, H. He, J. Yu, Y. Cui, Y. Yang and G. Qian, *Sci. China Chem.*, 2019, **62**, 987–993.
138 N. Zhang, D. Zhang, J. Zhao and Z. Xia, *Dalton Trans.*, 2019, **48**, 6794–6799.
139 Y. Liu, H. Dong, K. Wang, Z. Gao, C. Zhang, X. Liu, Y. S. Zhao and F. Hu, *ACS Appl. Mater. Interfaces*, 2018, **10**, 35455–35461.
140 B. Ruan, H.-L. Liu, L. Xie, H. Ding, Y. Zhang, J. Wu, Z. Huang, D. Shi, T. Jiang and F.-C. Tsai, *J. Fluoresc.*, 2020, **30**, 427–435.
141 Y. Wen, T. Sheng, X. Zhu, C. Zhuo, S. Su, H. Li, S. Hu, Q. L. Zhu and X. Wu, *Adv. Mater.*, 2017, **29**, 1700788.
142 V. Glembockyte, M. Frenette, C. Mottillo, A. M. Durantini, J. Gostick, V. Štrukil, T. Friščić and G. Cosa, *J. Am. Chem. Soc.*, 2018, **140**, 16882–16887.
143 S. Let, P. Samanta, S. Dutta and S. K. Ghosh, *Inorganica Chim. Acta*, 2020, **500**, 119205.
144 Y. Cui, R. Song, J. Yu, M. Liu, Z. Z. Z. Wang, C. Wu, Y. Yang, Z. Z. Z. Wang, B. Chen and G. Qian, *Adv. Mater.*, 2015, **27**, 1420–1425.
145 N. B. Shustova, T. C. Ong, A. F. Cozzolino, V. K. Michaelis, R. G. Griffin and M. Dincă, *J. Am. Chem. Soc.*, 2012, **134**, 15061–15070.
146 N. B. Shustova, A. F. Cozzolino and M. Dincă, *J. Am. Chem. Soc.*, 2012, **134**, 19596–19599.
147 H. Ding, J. Li, G. Xie, G. Lin, R. Chen, Z. Peng, C. Yang, B. Wang, J. Sun and C. Wang, *Nat. Commun.*, 2018, **9**, 5234.
148 N. B. Shustova, B. D. McCarthy and M. Dincă, *J. Am. Chem. Soc.*, 2011, **133**, 20126–20129.
149 N. B. Shustova, A. F. Cozzolino, S. Reineke, M. Baldo and M. Dincă, *J. Am. Chem. Soc.*, 2013, **135**, 13326–13329.
150 D. E. Williams, E. A. Dolgopolova, P. J. Pellechia, A. Palukoshka, T. J. Wilson, R. Tan, J. M. Maier, A. B. Greytak, M. D. Smith, J. A. Krause and N. B. Shustova, *J. Am. Chem. Soc.*, 2015, **137**, 2223–2226.
151 P. Deria, J. E. Mondloch, O. Karagiaridi, W. Bury, J. T. Hupp and O. K. Farha, *Chem. Soc. Rev.*, 2014, **43**, 5896–5912.
152 B. Wang, R.-B. Lin, Z. Zhang, S. Xiang and B. Chen, *J. Am. Chem. Soc.*, 2020, **142**, 14399–14416.
153 R. Haldar, A. Mazel, M. Krstić, Q. Zhang, M. Jakoby, I. A. Howard, B. S. Richards, N. Jung, D. Jacquemin, S. Diring, W. Wenzel, F. Odobel and C. Wöll, *Nat. Commun.*, 2019, **10**, 2048.
154 E. D. Spoerke, L. J. Small, M. E. Foster, J. Wheeler, A. M. Ullman, V. Stavila, M. Rodriguez and M. D. Allendorf, *J. Phys. Chem. C*, 2017, **121**, 4816–4824.
155 M. A. Gordillo, D. K. Panda and S. Saha, *ACS Appl. Mater. Interfaces*, 2019, **11**, 3196–3206.
156 S. Y. Ding, M. Dong, Y. W. Wang, Y. T. Chen, H. Z. Wang, C. Y. Su and W. Wang, *J. Am. Chem. Soc.*, 2016, **138**, 3031–3037.
157 P. Albacete, J. I. Martínez, X. Li, A. López-Moreno, S. Mena-Hernando, A. E. Platero-Prats, C. Montoro, K. P. Loh, E. M. Pérez and F. Zamora, *J. Am. Chem. Soc.*, 2018, **140**, 12922–12929.
158 H.-Q. Q. Yin, F. Yin and X.-B. B. Yin, *Chem. Sci.*, 2019, **10**, 11103–11109.
159 Z. Zhao, B. He and B. Z. Tang, *Chem. Sci.*, 2015, **6**, 5347–5365.
160 V. Vij, V. Bhalla and M. Kumar, *Chem. Rev.*, 2016, **116**, 9565–9627.
161 X. Feng, B. Tong, J. Shen, J. Shi, T. Han, L. Chen, J. Zhi, P. Lu, Y. Ma and Y. Dong, *J. Phys. Chem. B*, 2010, **114**, 16731–16736.
162 T. Han, X. Feng, J. Shi, B. Tong, Y. Dong, J. W. Y. Lam, Y. Dong and B. Z. Tang, *J. Mater. Chem. C*, 2013, **1**, 7534–7539.
163 Z. Wei, Z. Y. Gu, R. K. Arvapally, Y. P. Chen, R. N. McDougald, J. F. Ivy, A. A. Yakovenko, D. Feng, M. A. Omary and H.-C. Zhou, *J. Am. Chem. Soc.*, 2014, **136**, 8269–8276.
164 R. T. K. Kwok, C. W. T. Leung, J. W. Y. Lam and B. Z. Tang, *Chem. Soc. Rev.*, 2015, **44**, 4228–4238.
165 J. Chen, X. Chen, Q. Huang, W. Li, Q. Yu, L. Zhu, T. Zhu, S. Liu and Z. Chi, *ACS Appl. Mater. Interfaces*, 2019, **11**, 32689–32696.
166 Y. L. Ying, Y. J. Li, J. Mei, R. Gao, Y. X. Hu, Y. T. Long and H. Tian, *Nat. Commun.*, 2018, **9**, 3657.
167 Y. Li, Z. Xu, X. Zhu, B. Chen, Z. Wang, B. Xiao, J. W. Y. Lam, Z. Zhao, D. Ma and B. Z. Tang, *ACS Appl. Mater. Interfaces*, 2019, **11**, 17592–17601.
168 M. Yu, R. Huang, J. Guo, Z. Zhao and B. Z. Tang, *PhotoniX*, 2020, **1**, 11.
169 B. Zhang, J. L. Banal, D. J. Jones, B. Z. Tang, K. P. Ghiggino and W. W. H. Wong, *Mater. Chem. Front.*, 2018, **2**, 615–619.
170 G. Lyu, J. Kendall, I. Meazzini, E. Preis, S. Bayseç, U. Scherf, S. Clément and R. C. Evans, *ACS Appl. Polym. Mater.*, 2019, **1**, 3039–3047.

171 J. Mei, N. L. C. Leung, R. T. K. Kwok, J. W. Y. Lam and B. Z. Tang, *Chem. Rev.*, 2015, **115**, 11718–11940.
172 J. Dong, P. Shen, S. Ying, Z. J. Li, Y. Di Yuan, Y. Wang, X. Zheng, S. B. Peh, H. Yuan, G. Liu, Y. Cheng, Y. Pan, L. Shi, J. Zhang, D. Yuan, B. Liu, Z. Zhao, B. Z. Tang and D. Zhao, *Chem. Mater.*, 2020, **32**, 6706–6720.
173 S. Choi, H.-E. Lee, C. H. Ryu, J. Lee, J. Lee, M. Yoon, Y. Kim, M. H. Park, K. M. Lee and M. Kim, *Chem. Commun.*, 2019, **55**, 11844–11847.
174 H. Wang, E. Zhao, J. W. Y. Lam and B. Z. Tang, *Mater. Today*, 2015, 18, 365–377.
175 H.-T. Feng, Y.-X. Yuan, J.-B. Xiong, Y.-S. Zheng and B. Z. Tang, *Chem. Soc. Rev.*, 2018, **47**, 7452–7476.
176 Z. Yang, Z. Chi, Z. Mao, Y. Zhang, S. Liu, J. Zhao and J. Zhao, *Mater. Chem. Front.*, 2018, **2**, 861–890.
177 B. Jiang, C.-W. Zhang, X.-L. Shi and H.-B. Yang, *Chinese J. Polym. Sci.*, 2019, **37**, 372–382.
178 D.-H. Wang, D.-J. Zhu, W. Ding, M. Xue and Y. Yang, *Org. Biomol. Chem.*, 2018, **16**, 4429–4432.
179 X. Feng, C. Qi, H.-T. Feng, Z. Zhao, H. H. Y. Sung, I. D. Williams, R. T. K. Kwok, J. W. Y. Lam, A. Qin and B. Z. Tang, *Chem. Sci.*, 2018, **9**, 5679–5687.
180 J. Guan, R. Wei, A. Prlj, J. Peng, K.-H. Lin, J. Liu, H. Han, C. Corminboeuf, D. Zhao, Z. Yu and J. Zheng, *Angew. Chem. Int. Ed.*, 2020, **59**, 14903–14909.
181 Q. Gao, X. Li, G.-H. Ning, K. Leng, B. Tian, C. Liu, W. Tang, H.-S. Xu and K. P. Loh, *Chem. Commun.*, 2018, **54**, 2349–2352.
182 Y. Hong, J. W. Y. Lam and B. Z. Tang, *Chem. Soc. Rev.*, 2011, **40**, 5361–5388.
183 L. Ma, X. Feng, S. Wang and B. Wang, *Mater. Chem. Front.*, 2017, **1**, 2474–2486.
184 J. Xiong, X. Qian, L. Zhao and J. Xu, *Inorg. Chem. Commun.*, 2019, **105**, 20–25.
185 C.-L. Tao, B. Chen, X.-G. Liu, L.-J. Zhou, X.-L. Zhu, J. Cao, Z.-G. Gu, Z. Zhao, L. Shen and B. Z. Tang, *Chem. Commun.*, 2017, **53**, 9975–9978.
186 X. Zhao, Y. Li, Z. Chang, L. Chen and X.-H. Bu, *Dalton Trans.*, 2016, **45**, 14888–14892.
187 X.-H. Wu, P. Luo, Z. Wei, Y.-Y. Li, R.-W. Huang, X.-Y. Dong, K. Li, S.-Q. Zang and B. Z. Tang, *Adv. Sci.*, 2019, **6**, 1801304.
188 M. M. Islam, Z. Hu, Q. Wang, C. Redshaw and X. Feng, *Mater. Chem. Front.*, 2019, **3**, 762–781.
189 N. Nirmalananthan, T. Behnke, K. Hoffmann, D. Kage, C. F. Gers-Panther, W. Frank, T. J. J. Müller and U. Resch-Genger, *J. Phys. Chem. C*, 2018, **122**, 11119–11127.
190 L. Biesen, N. Nirmalananthan-Budau, K. Hoffmann, U. Resch-Genger and T. J. J. Müller, *Angew. Chem. Int. Ed.*, 2020, **59**, 10037–10041.
191 D. D. La, S. V. Bhosale, L. A. Jones and S. V. Bhosale, *ACS Appl. Mater. Interfaces*, 2018, **10**, 12189–12216.
192 H. Tong, Y. Hong, Y. Dong, M. Häußler, J. W. Y. Lam, Z. Li, Z. Guo, Z. Guo and B. Z. Tang, *Chem. Commun.*, 2006, 3705–3707.
193 W. P. Lustig, Z. Shen, S. J. Teat, N. Javed, E. Velasco, D. M. O'Carroll and J. Li, *Chem. Sci.*, 2020, **11**, 1814–1824.
194 Z.-F. Wu, E. Velasco, C. Shan, K. Tan, Z.-Z. Zhang, Q.-Q. Hu, K. Xing, X.-Y. Huang and J. Li, *J. Mater. Chem. C*, 2020, **8**, 6820–6825.
195 F.-M. Wang, L. Zhou, W. P. Lustig, Z. Hu, J.-F. Li, B.-X. Hu, L.-Z. Chen and J. Li, *Cryst. Growth Des.*, 2018, **18**, 5166–5173.
196 N. D. Rudd, H. Wang, S. J. Teat and J. Li, *Inorganica Chim. Acta*, 2018, **470**, 312–317.
197 L. Yu, H. Wang, W. Liu, S. J. Teat and J. Li, *Cryst. Growth Des.*, 2019, **19**, 6850–6854.
198 Y. Guo, X. Feng, T. Han, S. Wang, Z. Lin, Y. Dong and B. Wang, *J. Am. Chem. Soc.*, 2014, **136**, 15485–15488.
199 Y. Zhang, T. Han, S. Gu, T. Zhou, C. Zhao, Y. Guo, X. Feng, B. Tong, J. Bing, J. Shi, J. Zhi and Y. Dong, *Chem. Eur. J.*, 2014, **20**, 8856–8861.
200 T. Han, Y. Zhang, X. Feng, Z. Lin, B. Tong, J. Shi, J. Zhi and Y. Dong, *Chem. Commun.*, 2013, **49**, 7049–7051.
201 S. Dalapati, E. Jin, M. Addicoat, T. Heine and D. Jiang, *J. Am. Chem. Soc.*, 2016, **138**, 5797–5800.
202 A. M. Evans, I. Castano, A. Brumberg, L. R. Parent, A. R. Corcos, R. L. Li, N. C. Flanders, D. J. Gosztola, N. C. Gianneschi, R. D. Schaller and W. R. Dichtel, *J. Am. Chem. Soc.*, 2020, **141**, 19728–19735.
203 E. Jin, J. Li, K. Geng, Q. Jiang, H. Xu, Q. Xu and D. Jiang, *Nat. Commun.*, 2018, **9**, 4143.
204 D. Rota Martir and E. Zysman-Colman, *Chem. Commun.*, 2019, **55**, 139–158.
205 S. Durot, J. Taesch and V. Heitz, *Chem. Rev.*, 2014, **114**, 8542–8578.
206 P. P. Neelakandan, A. Jiménez and J. R. Nitschke, *Chem. Sci.*, 2014, **5**, 908–915.
207 C. Bravin, G. Mason, G. Licini and C. Zonta, *J. Am. Chem. Soc.*, 2019, **141**, 11963–11969.
208 J. R. Piper, L. Cletheroe, C. G. P. Taylor, A. J. Metherell, J. A. Weinstein, I. V. Sazanovich and M. D. Ward, *Chem. Commun.*, 2017, **53**, 408–411.